

Decoding dark matter at future e^+e^- colliders

Alexander Belyaev^{1,2,*} Arran Freegard^{1,†} Ilya F. Ginzburg^{3,‡} Daniel Locke^{1,§} and Alexander Pukhov^{1,4,||}

¹*School of Physics and Astronomy, University of Southampton, Southampton SO17 1BJ, United Kingdom*

²*Particle Physics Department, Rutherford Appleton Laboratory, Chilton, Didcot, Oxon OX11 0QX, United Kingdom*

³*Sobolev Institute of Mathematics, Novosibirsk, 630090, Russia and Novosibirsk State University, Novosibirsk 630090, Russia*

⁴*Skobeltsyn Institute of Nuclear Physics, Moscow State University, Moscow 119992, Russia*



(Received 24 January 2022; accepted 23 June 2022; published 19 July 2022)

We explore the potential of the e^+e^- colliders to discover dark matter and determine its properties such as mass and spin. For this purpose we study spin zero and spin one-half cases of dark matter D , which belongs to the $SU(2)$ weak doublet and therefore has the charged doublet partner D^+ . For the case of scalar dark matter we chose inert doublet model, while for the case of fermion dark matter we suggest the new minimal fermion dark matter model with only three parameters. We choose two benchmarks for the models under study, which provide the correct amount of observed dark matter (DM) relic density and consistent with the current DM searches. We focus on the particular process $e^+e^- \rightarrow D^+D^- \rightarrow DDW^+W^- \rightarrow DD(q\bar{q})(\mu^\pm\nu)$ at the 500 GeV ILC collider that gives rise to the “dijet + μ + \cancel{E}_T ” signature and study it at the level of fast detector simulation, taking into account bremsstrahlung and ISR effects. We have found that two kinematical observables—the energy of the muon E_μ and the angular distribution of the W boson, reconstructed from dijet $\cos\theta_{jj}$ are very powerful in determination of DM mass and spin, respectively. In particular we have demonstrated that in the case of fermion DM, the masses can be measured with a few percent accuracy already at 500 fb^{-1} integrated luminosity. At the same time, the scalar DM model which has about an order of magnitude lower signal, requires about a factor of 40 higher luminosity to reach the same accuracy in the mass measurement. We have found that one can distinguish fermion and scalar DM scenarios with about 2 ab^{-1} total integrated luminosity or less without using the information on the cross sections for benchmarks under study. The methods of the determination of DM properties which we suggest here are generic for the models where DM and its partner belong to the weak multiplet and can be applied to explore various DM models at future e^+e^- colliders.

DOI: [10.1103/PhysRevD.106.015016](https://doi.org/10.1103/PhysRevD.106.015016)

I. INTRODUCTION

The search for dark matter (DM) in high energy physics (HEP) experiments has become one of the primary goals of the LHC and future colliders, in addition to noncollider experiments. Indeed it is one of the fundamental problems for the HEP community to discover and decode the nature of DM, the existence of which has been confirmed by several independent cosmological observations.

These include galactic rotation curves, cosmic microwave background fits of the WMAP and PLANCK data, gravitational lensing, the large scale structure of the Universe, and interacting galaxy clusters such as the bullet cluster. Despite this multitude of observations strongly suggesting the existence of cold nonbaryonic particle DM, many of its properties remain a mystery. We do not know what is the spin and the mass of DM, whether it is involved in nongravitational interactions, what symmetry stabilizes any partner of DM particles in the dark sector.

As one of the most active research areas in HEP, there are many key papers exploring the vast model landscape of DM and the possibilities to disentangle these models experimentally. DM models under study include SUSY [1–3], sterile neutrinos [4], general minimal WIMP models [5], Axions [6], Kaluza-Klein DM [7], universal extra dimensions [8], and extended Higgs sectors [9–11]. Determination of DM properties such as spin [12–14] and mass [15,16] would be key in the event of a discovery.

*a.belyaev@soton.ac.uk

†acf1g14@soton.ac.uk

‡ginzburg@math.nsc.ru

§D.R.Locke@soton.ac.uk

||pukhov@lapp.in2p3.fr

Published by the American Physical Society under the terms of the [Creative Commons Attribution 4.0 International license](https://creativecommons.org/licenses/by/4.0/). Further distribution of this work must maintain attribution to the author(s) and the published article's title, journal citation, and DOI. Funded by SCOAP³.

Traditional searches for DM at the LHC via missing energy signatures through monojet [17,18], mono- $Z(W)$ [19–24], mono-Higgs [25–29], DM+ top quarks [30–32], and invisible Higgs decays [23,33,34] or through potential mediators [35–37] expand on constraints from Large Electron-Positron (LEP) collider on DM charged partner masses [38]. DM may also be probed in scenarios where its charged partners are long-lived, providing unique signatures with little background. These scenarios, known as nonprompt searches, include disappearing charged tracks [39,40] and displaced vertices [41,42].

In the case of generic scenarios where DM is involved in $SU(2)$ electroweak (EW) interactions and no additional beyond-the-standard-model (BSM) mediators are present, it is quite challenging for the LHC to probe such a DM even in the 100 GeV range. For example, in [43] it was shown that even at the high luminosity (HL) LHC, the Higgsino-like neutralino DM from the Minimal Supersymmetric Standard Model (MSSM) can be probed only up to about 200 GeV mass with very high transverse momentum monojet signature required to reduce the large SM background. There are no current constraints on such a scenario from the LHC and the best limits are set up by LEP on charged DM partner (e.g., chargino) mass to be above 100 GeV [43].

The most recent global scans of the MSSM [44] including the neutralino and chargino sector (analogous to split SUSY scenarios) [45] reveal a best fit region consistent with a higgsino-bino DM candidate, which is mostly bino (mostly singlet DM will avoid direct detection constraints). These viable points rely on the so-called ‘‘Higgs funnel’’ annihilation channel (DM mass around half Higgs mass) in order to reproduce the relic density as measured by PLANCK. Such scenarios may be ideally probed by a e^+e^- 500 GeV collider such as the ILC, where the accessible particle spectrum (< 300 GeV) contains the two lightest neutralinos in addition to the lightest chargino.

In this study we explore the potential of a future e^+e^- collider to probe and distinguish two well-motivated minimal models with DM of spin-0 and spin-1/2 embedded into an $SU(2)$ weak doublet with no additional BSM mediator. We assume that the DM sector is represented by an EW doublet without loss of generality and that each model includes DM D , its charged partner D^+ , and heavier neutral partner(s) D_2 with $M_{D_2} > M_D$, which are odd particles with respect to the Z_2 symmetry responsible for DM stability. We explore the potential of the 500 GeV e^+e^- collider (which can be ILC, FCC-ee, CLIC, etc.) to measure M_D and M_+ masses and distinguish DM spin using semileptonic signature from D^+D^- decays. The observation of such signature requires a nonvanishing mass gap $\Delta M = M_+ - M_D (\gtrsim 10$ GeV) which would provide detectable leptons.

There are several important advantages of the e^+e^- colliders in comparison to the LHC which motivate our

study, including (a) the background cross section at e^+e^- collider is lower and the respective signal to background ratio is at least 1 order of magnitude higher than the one at the LHC; (b) at e^+e^- colliders one can determine not only the missing transverse momentum, but also missing mass, which allows us to further suppress the background without reducing the signal; (c) since the center-of-mass energy is fixed at e^+e^- colliders, they allow us to reconstruct kinematics of various particles and their distributions in the lab frame, including characteristics of W^\pm bosons from D^\pm decays which is crucial for determination of DM properties as we demonstrate in our paper.

Our study goes beyond the previous exploration (e.g., Refs. [14] or [46]) of the ILC potential to discriminate DM models in several principal aspects: (a) we explore models with DM of two different spins and for the first time demonstrate that W -boson angular distribution allows us to determine the spin of DM even without using the information about the signal cross section; (b) we explore the signature with leptonic final state which has the advantage of keeping the background under better control and more precise determination of the final state energy distributions; (c) we make use of the predicted cross sections for typical parameter points delivering the correct relic abundance; (d) we suggest the set of new kinematical observables and cuts which boost e^+e^- collider potential discrimination of DM models; (e) we explore both cases for off-shell and on-shell W -boson decay; (f) we use a model-independent template-based approach to fit kinematic end points and determine D and D^+ masses using likelihood methods. In addition, for the case of fermion DM we suggest the new minimal fermion dark matter (MFDm) model with only three parameters.

This paper is organized as following. In Sec. II we discuss models, benchmarks, and analysis setup, in Sec. III we study the signal properties, in Sec. IV we perform signal versus background analysis and find the potential of the e^+e^- collider to determine DM properties, such as mass and spin. Finally in Sec. V we draw our conclusions.

II. MODELS AND BENCHMARKS

A. Inert doublet model (I2HDM)

The spin-0 or scalar DM (SDM) model which we use as a first case study is the inert two Higgs doublet model [47–53], which in addition to the SM Higgs doublet contains the inert scalar Z_2 -odd doublet, ϕ_D , that does not acquire a vacuum expectation value (VEV). In our paper we call all particles odd under Z_2 symmetry D particles, and refer to the Z_2 symmetry as D parity. The scalar sector of the model is given by

$$\mathcal{L} = |D_\mu \Phi|^2 + |D_\mu \phi_D|^2 - V(\Phi, \phi_D), \quad (1)$$

where V is the potential with all scalar interactions compatible with the Z_2 symmetry:

$$\begin{aligned}
 V = & -m_1^2(\Phi^\dagger\Phi) - m_2^2(\phi_D^\dagger\phi_D) + \lambda_1(\Phi^\dagger\Phi)^2 + \lambda_2(\phi_D^\dagger\phi_D)^2 \\
 & + \lambda_3(\Phi^\dagger\Phi)(\phi_D^\dagger\phi_D) + \lambda_4(\phi_D^\dagger\Phi)(\Phi^\dagger\phi_D) \\
 & + \frac{\lambda_5}{2}[(\Phi^\dagger\phi_D)^2 + (\phi_D^\dagger\Phi)^2]. \quad (2)
 \end{aligned}$$

In the unitary gauge, the SM doublet, Φ and the inert doublet, ϕ_D take the form

$$\Phi = \frac{1}{\sqrt{2}} \begin{pmatrix} 0 \\ v + H \end{pmatrix}, \quad \phi_D = \frac{1}{\sqrt{2}} \begin{pmatrix} \sqrt{2}D^+ \\ D + iD_2 \end{pmatrix}, \quad (3)$$

where we consider the parameter space in which only the first, SM-like doublet, acquires a VEV, v . After EW symmetry breaking (EWSB), the D parity is still conserved by the vacuum state, which forbids direct coupling of any single inert field to the SM fields and protects the lightest inert boson from decaying, hence providing the DM candidate in this scenario. In addition to the SM-like scalar H , the model contains one inert charged D^+ and two further inert neutral D and D_2 scalars. The two neutral scalars of the I2HDM have opposite CP parities, but it is impossible to unambiguously determine which of them is CP even and which one is CP odd since the model has two CP symmetries, $D \rightarrow D, D_2 \rightarrow -D_2$ and $D \rightarrow -D, D_2 \rightarrow D_2$, which get interchanged upon a change of basis $\phi_D \rightarrow i\phi_D$. This makes the specification of the CP properties of D and D_2 a basis-dependent statement. Therefore, following Ref. [11], we denote the two neutral inert scalar masses as $M_D < M_{D_2}$, without specifying which is scalar or pseudo-scalar, so that D is the DM candidate.

The model can be conveniently described by a five-dimensional parameter space [11] using the following phenomenologically relevant variables:

$$M_D, \quad M_{D_2} > M_D, \quad M_+ > M_D, \quad \lambda_2 > 0, \quad \lambda_{345} > -2\sqrt{\lambda_1\lambda_2}, \quad (4)$$

where M_D, M_{D_2} and M_+ are the masses of the two neutral and charged inert scalars, respectively, whereas $\lambda_{345} = \lambda_3 + \lambda_4 + \lambda_5$ is the coupling that governs the Higgs-DM interaction vertex HDD . There is $(\phi_D \rightarrow i\phi_D, \lambda_5 \rightarrow -\lambda_5)$ symmetry of the Lagrangian which allows us to chose $\lambda_5 > 0$ as a convention. The masses of the three inert scalars are expressed in terms of the parameters of the Lagrangian in Eqs. (1)–(2) as follows:

$$\begin{aligned}
 M_D^2 &= \frac{1}{2}(\lambda_3 + \lambda_4 - \lambda_5)v^2 - m_2^2, \\
 M_{D_2}^2 &= \frac{1}{2}(\lambda_3 + \lambda_4 + \lambda_5)v^2 - m_2^2 > M_D^2, \\
 M_+^2 &= \frac{1}{2}\lambda_3 v^2 - m_2^2, \quad (5)
 \end{aligned}$$

which represent the only three parameters relevant to our study, since we explore production of D particles in the gauge interactions at e^+e^- colliders.

Constraints on the Higgs potential from requiring vacuum stability and a global minimum take the following form [11]:

$$\begin{cases} M_D^2 > 0 & \text{(the trivial one)} & \text{for } |R| < 1, \\ M_D^2 > (\lambda_{345}/2\sqrt{\lambda_1\lambda_2} - 1)\sqrt{\lambda_1\lambda_2}v^2 = (R - 1)\sqrt{\lambda_1\lambda_2}v^2 & \text{for } R > 1, \end{cases} \quad (6)$$

where $R = \lambda_{345}/2\sqrt{\lambda_1\lambda_2}$ and $\lambda_1 \approx 0.129$ is fixed as in the SM by the Higgs mass in Eq. (5). The latter condition places an important upper bound on λ_{345} for a given DM mass M_D . Constraints on the model's parameter space have already been comprehensively explored in a large variety of previous papers [11,47–50,54–75].

B. Minimal Fermion DM (MFDM)

The second model we consider here is a minimal model with an EW fermion DM doublet. The model should respect direct DM constraints coming from the most restrictive DM direct detection (DD) searches from the XENON1T experiment [76], and at the same time provide the correct amount (or at least not an overabundance) of relic density. Therefore the model must have a mechanism to suppress DM scattering through intermediate Z bosons and/or Higgs bosons. Among several candidates for such a

mechanism, the most minimal is to introduce Majorana neutral D -odd particles χ_1^0 and χ_2^0 as a part of an EW doublet and split their masses via interactions with the SM Higgs doublet and additional Majorana singlet fermion χ_s^0 :

$$\begin{aligned}
 \mathcal{L}_{\text{FDM}} = & \mathcal{L}_{\text{SM}} + \bar{\psi}(i\not{D} - m_\psi)\psi + \frac{1}{2}\bar{\chi}_s^0(i\not{\partial} - m_s)\chi_s^0 \\
 & - (Y(\bar{\psi}\Phi\chi_s^0) + \text{H.c.}), \quad (7)
 \end{aligned}$$

where fermion fields are in bispinor form and Φ is the SM Higgs doublet. A DM $SU(2)$ vectorlike doublet with hypercharge $Y = 1/2$, may be defined in terms of majorana states χ^0, χ'^0 as

$$\psi = \begin{pmatrix} \chi^+ \\ \frac{1}{\sqrt{2}}(\chi^0 + i\chi'^0) \end{pmatrix}. \quad (8)$$

The model which we suggest and use in our paper has only three new parameters: m_ψ , Y , and m_s . This model is more minimal in comparison to the previously studied doublet-singlet model [77,78] which has four parameters because of *two* Yukawa couplings, distinguishing left- and right-handed interactions of Higgs and DM doublets with χ_s^0 . Our choice of the parity conserving $\psi - \Phi - \chi_s^0$ Yukawa interactions adds just one parameter to the model—the Yukawa coupling, which is the same for left and right interactions. We have checked that this scenario is radiatively stable. This parity would be spoiled if the DM sector would directly couple to SM fermions, which is eventually not the case. Therefore our model with just three new parameters is consistent and truly the minimal one.

The Yukawa interaction mixes χ^0 and χ_s^0 while χ^+ and χ'^0 have the same mass m_ψ and remain degenerate at tree level. This degeneracy is not essential, since χ^0 decay is driven by the $\chi^0 \rightarrow \chi^0 Z^{(*)}$ process.

We trade m_ψ , Y and m_s parameters for three physical masses:

$$M_D, \quad m_\psi \equiv M_+ = M_{D'}, \quad \text{and} \quad M_{D_2}, \quad (9)$$

corresponding to (D, D_2, D') mass bases of the neutral DM sector, which one obtains from the diagonalization of the mass matrix in the $(\chi^0, \chi_s, \chi'^0)$ basis:

$$\mathcal{M} = \begin{bmatrix} m_\psi & Yv & 0 \\ Yv & m_s & 0 \\ 0 & 0 & m_\psi \end{bmatrix}. \quad (10)$$

Since the mass and gauge eigenstate of χ^0 coincide and have the mass $m_\psi \equiv M_+ = m_{D_2}$, diagonalization should be done only for 2×2 upper-left block of the matrix (10). This diagonalization describes the rotation of the gauge eigenstates (χ^0, χ_s^0) into the mass eigenstates (D, D_2) by angle θ and given by

$$\begin{aligned} \chi^0 &= D \cos \theta - D_2 \sin \theta, \\ \chi_s^0 &= D \sin \theta + D_2 \cos \theta. \end{aligned} \quad (11)$$

One can find the following useful relations from this diagonalization:

$$m_s = M_D + M_{D_2} - M_+, \quad (12)$$

$$\tan 2\theta = \frac{2Yv}{m_\psi - m_s} = \frac{2Yv}{2M_+ - M_{D_2} - M_D}, \quad (13)$$

$$\sin 2\theta = -\frac{2Yv}{M_{D_2} - M_D}. \quad (14)$$

The relation between Yukawa coupling, Y and physical mass parameters is given by

$$Y = \pm \frac{\sqrt{(M_{D_2} - M_+)(M_+ - M_D)}}{v}. \quad (15)$$

The mass order

$$M_{D_2} > M_+ = M_{D'} > M_D \quad (16)$$

follows from the condition for Y to be real. The phase of χ_s^0 may be chosen such that Y is positive. This MFDM model, with singlet-doublet dark sector content can be mapped into the bino-Higgsino MSSM model with all other SUSY particles decoupled, including winos.

In this model, DM interaction with the Z boson is absent at tree level. One should also note that inelastic upscatterings arising from the ZDD' vertex do not take place for the mass split between D and D' above the recoil energy threshold of direct detection experiments (typically around 1–10 keV)—the case of our study. The spin-independent DM—nucleon scattering cross section therefore depends only on the Higgs coupling to DM, g_{DDh} , given by

$$g_{DDh} = -2Y \cos \theta \sin \theta = 2 \frac{(M_+ - M_D)(M_{D_2} - M_+)}{v(M_{D_2} - M_D)}, \quad (17)$$

which follows from Eqs. (14) and (15). This coupling can be small, which provides viable parameter space from DM direct detection point of view. In this study we consider scenarios with relatively large $M_+ - M_D$ mass gap—of the order of W -boson mass, so D^+ decays to on-shell (or slightly virtual) W bosons. In this scenario, the small value of g_{DDh} coupling is driven by the small $M_{D_2} - M_+$ value as one can see from Eq. (17). At the same time the correct relic abundance can be provided through the effective resonant annihilation of DM through the Higgs boson, when $M_D \simeq M_h/2$ even if the value of g_{DDh} is small. One should note that in this case $D - D_2$ and $D - D^+$ co-annihilation channels are subdominant due to the relatively large mass split between DM and its partners. The implementation of this model in the CalcHEP [79] format using the LanHEP package [80] is publicly available in the High Energy Model Physics database (HEPMDB) [81] at [82].

C. Benchmark points

In our study we chose two benchmarks with different $D^+ - D$ mass gaps: one—providing $D^+ \rightarrow DW$ decay with on-mass-shell W boson in the final state and another—with the off-mass-shell W^* boson. We choose model parameters providing the right amount of relic density and satisfying the latest DM DD constraint from XENON1T searches to make sure that chosen benchmarks are the realistic ones. The benchmarks are presented in Table I together with DM observables, where abbreviations SDM and FDm denote scalar and fermion DM, respectively. One should note that

TABLE I. Benchmark points for I2HDM and MFDM with DM observables. All masses are given in GeV. Abbreviations SDM and FDM denote scalar and fermion DM, respectively.

Parameters	Benchmarks		
	BP1	BP2	
M_D	60	60	
M_+	160	120	
M_{D_2}	160.85	120.85	
I2HDM parameters			
λ_{345}	6.5×10^{-4}	7.0×10^{-4}	
λ_2	1.0	1.0	
DM observables			
Ωh^2	SDM	0.111	0.112
	FDM	0.108	0.109
σ_{SI}^p [pb]	SDM	6.17×10^{-13}	6.17×10^{-13}
	FDM	1.67×10^{-11}	1.65×10^{-11}

I2HDM model has two more parameters (five versus three) in comparison to MFDM model— λ_{345} and λ_2 . First we chose M_D, M_D^+, M_{D_2} to make the relic density consistent with the results from PLANCK for MFDM model, then use additional parameter λ_{345} from I2HDM to make the relic density from this model to be consistent with PLANCK. The other parameter— λ_2 , which controls the self-interaction of DM, is not relevant to collider phenomenology. We keep $\lambda_2 = 1$ without loss of generality¹ since it does not affect any conclusion in this paper. We chose the same D, D^+ , and D_2 masses for both models with the aim to explore the ILC potential in distinguishing theories with the same mass but different spin of the DM sector.

The relic density Ωh^2 and spin-independent proton scattering cross section σ_{SI}^p were calculated using the micrOMEGAs package [83].

We have recast an existing SUSY analysis using CheckMATE2 [84] and found that the most sensitive search for BP1 and BP2 is the CMS 13 TeV search for electroweak production of charginos and neutralinos in multilepton final states [85]. CheckMATE evaluates the r number defined as a ratio of the signal cross section and the cross section excluded at 95% Confidence Level (CL), so $r = 1$ means that the model is excluded at 95% CL. The respective values for BP1 and BP2 are found to be 0.325 and 0.664, respectively, which means that these points are still allowed by the LHC data.² Many of the most stringent LHC constraints on electroweak scale WIMP masses arise

¹The large value of the λ_2 could potentially affect the DM density profile and loop-induced DM annihilation into SM particles. These effects are outside the scope of this paper.

²The latest CheckMATE2 sensitivity could be a bit higher since the time our analysis was done.

from decays mediated by sleptons and sneutrinos of mass $\gtrsim 500$ GeV. In the scenarios explored here we assume that all additional SUSY particles (or analogous particles which could appear in the I2HDM extension) are decoupled. It is worth noting that the global scan of electroweakino DM by the GAMBIT Collaboration shows favored parameter points around our benchmarks [45].

For the models under study one should also respect the constraints from the electroweak precision test (EWPT). EWPT quantities include S, T , and U observables that parametrize contributions from beyond standard model physics to electroweak radiative corrections [86]. For I2HDM the expressions for the S and T parameters are evaluated in [48,61] and give

$$S = -0.016(-0.013), \quad T = -0.00146(-0.00090) \quad (18)$$

values for BP1(BP2), respectively. The contribution to the U parameter for I2HDM can be neglected. These S and T values for our benchmarks are allowed by the current EWPT fits which (with U fixed to be zero), have the following central values (for SM Higgs boson mass 125 GeV) [87]:

$$S = -0.01 \pm 0.07, \quad T = 0.04 \pm 0.06, \quad (19)$$

with correlation coefficient +0.91. For MFDM we have derived the expressions for S and T and present them in Appendix A. For MFDM the values of the S parameter are

$$S = -1.06 \times 10^{-4}(-8.38 \times 10^{-5}) \quad (20)$$

for BP1(BP2) respectively, while the T and U parameters are explicitly zero. This happens because one of the down parts of the vectorlike doublet, corresponding to the neutral Majorana fermion, does not mix and has the same mass as the charged fermion. For details we refer the reader to Appendix A. To conclude, the benchmarks for both models are consistent with the EWPT, which is expected since the mass split between vectorlike fermions is not large and the S and T parameters are proportional to the mass split squared (in case if they are not explicitly zero like the T parameter in MFDM). We would like also to note that contrary to the case of doublet of new chiral fermions, the T parameter for which is known for more than 40 years [88,89], the T parameter for vectorlike fermions is model dependent. Therefore, we would like to stress that the general statement in the Review of Particle Physics (PDG) [87] that vectorlike fermion doublets contribute to T with an extra factor of 2 is not correct in general.

D. Analysis setup

In our study we use the following tools to evaluate the ILC potential to probe properties of DM. We use CalcHEP [79] to perform the parton-level signal analysis in Sec. III,

including the study of the finite width effects from W -boson decay, and the effects from the initial state radiation (ISR) and beamstrahlung radiation (B).³ We use Pythia8 [91] to simulate final state radiation and hadronization effects. Events from Pythia are then passed to the Delphes [92] fast-detector simulator using the ILC card based on the proposed ILD detector [90]. We have used the anti- K_T jet clustering algorithm [93] with the value of radius parameter R set to 0.8 (instead of its default 0.5) which allows us to add the additional soft jets and improve dijet reconstruction. At this level of simulation we have performed signal and background analysis of the various kinematic distributions to extract D and D^+ masses to distinguish scalar and fermion DM models as discussed in detail in Sec. III. D.

III. THE PROPERTIES OF DM SIGNAL AT THE e^+e^- COLLIDER

In this section, we discuss and develop the generic strategies which we suggest to employ in order to discern the masses and spin of DM in the classes of models discussed in the previous section. In order to evaluate the applicability of such strategies we examine the cross section of the relevant production channels and the dominant background processes. Besides, we also discuss various kinematical observables and the respective distributions which will be later used to discriminate DM properties and optimize signal versus background.

A. The signatures

The $e^+e^- \rightarrow D^+D^-$ process, followed by subsequent D^\pm decay to D and W and then by W decay to leptons or quarks lead to the following signatures:

- (i) *Two dijets + \cancel{E}_T* from the

$$e^+e^- \rightarrow D^+D^- \rightarrow DDW^+W^- \rightarrow DD(W^+ \rightarrow q\bar{q}') \times (W^- \rightarrow q\bar{q}') \quad (21)$$

process. This signature has large missing transverse mass \cancel{E}_T and large M_{miss} while each dijet cluster has energy $< \frac{\sqrt{s}}{2}$.

- (ii) *Dijet + (e or μ) + \cancel{E}_T* , with energy of each dijet or lepton $< \frac{\sqrt{s}}{2}$, with large \cancel{E}_T and large M_{miss} , which originates from the

$$e^+e^- \rightarrow D^+D^- \rightarrow DDW^+W^- \rightarrow DD(W \rightarrow \ell\nu) \times (W \rightarrow q\bar{q}) \quad (22)$$

process.

³In our setup we have used the ISR scale equal to the \sqrt{s} , $\sigma_x + \sigma_y = 500$ nm for bunch $x + y$ size, 0.3 mm for bunch length and 2×10^{10} particles in the bunch, corresponding to the standard setup for ILC simulation [90].

Here we consider the $M_+ < M_{D_2}$ case only, for which the branching fraction of $D^\pm \rightarrow DW^\pm$ decay is 100%. At $M_W^* > 5$ GeV, the branching ratios for different channels of W^* decay are roughly identical to those for on-shell W [94]. In particular, the fraction of events with signature (21) is $0.676^2 \approx 0.45$. The fraction of events with signature (22) is $2 \cdot 0.676 \cdot (2 + 0.17) \cdot 0.108 \approx 0.32$ (here 0.17 is a fraction of μ or e from τ decay). At $M_W^* < 5$ GeV the branchings $\text{BR}(e\nu)$ and $\text{BR}(\mu\nu)$ increase, while the dijet becomes a set of a few hadrons.

One should also mention, that in case when $M_+ > M_{D_2}$ (which we do not study here), D_2 contributes to D^\pm decay such as

$$D^\pm \rightarrow D_2W^\pm \rightarrow DZW^\pm, \quad (23)$$

which gives rise to the additional signatures such as

- (i) *from (4 dijets, 0 charged leptons) to (1 dijet, 5 charged leptons)*,

originating from

$$e^+e^- \rightarrow D^+D^- \rightarrow DW^+D_2W^- \rightarrow DDW^+W^-Z \quad (24)$$

and

$$e^+e^- \rightarrow D^+D^- \rightarrow D_2W^+D_2W^- \rightarrow DDW^+W^-ZZ \quad (25)$$

cascade processes. Note that the processes with invisible decay $Z \rightarrow \nu\bar{\nu}$ (with branching fraction $BR = 20\%$) have the same signature as processes (21) and (22). There is also an additional process leading to D -odd particles + leptons in the final state, $e^+e^- \rightarrow DD_2 \rightarrow DDZ$ which we discuss in Appendix B in the details.

In our study we denote electron beam energy as

$$E = \sqrt{s}/2. \quad (26)$$

We consider energies E and three-momenta, \vec{p} , of particles in different reference systems and use particle name in superscript (W for W^+ and D for D^+) for energy and momentum to indicate their Lorentz frame. For the lab system (cms for e^+e^-) corresponding quantities are written without superscript. The subscript indicates just the name of the particle to which the physical quantity belongs. For example, $\vec{p}_W^{D^+}$ is value of three momentum of W^+ in the rest frame of D^+ , and E_μ is the energy of muon in the lab system.

We supply upper superscript by additional sign max, (+), (−) to characterize the values for the corresponding energy which we define in the text. The energy can depend on some parameters, e.g., the mass of a virtual W boson (M_W^*), which we indicate in brackets. For example, $E_\mu^{\text{max}}(M_W^*)$ means the maximum energy of the muon from the W^* with the M_W^* invariant mass.

B. Kinematical observables

We study the signal from DM originating from the $e^+e^- \rightarrow D^+D^-$ process, followed by D^\pm decay to D and on-shell or off-shell W^\pm , which we denote as W from now on for both (off-shell or on-shell) cases. In its turn, W decays to a $q\bar{q}$ pair (dijet) or $\ell\nu$.

Respectively, we will use several characteristic kinematical observables for the signal and background processes relevant to this final state.

- (i) Among them is the missing mass, M_{miss} which is invariant mass of the invisible particles system, i.e., invisible mass for a pair of DM particles, defined as

$$M_{\text{miss}} = \sqrt{\left((\sqrt{s}, 0, 0, 0) - \sum_{\text{vis}} P_{\text{vis}} \right)^2}, \quad (27)$$

where P_{vis} are 4-momenta of visible particles.

In the absence of the initial state radiation and beamstrahlung effects (which we call ISR + B effects for brevity from now on) the minimum value of M_{miss} is $2M_D$, while for SM background (BG) with just one neutrino in the final state M_{miss} is vanishing. Therefore, in this particular case BG can be perfectly separated from the signal using just one M_{miss} variable. In reality ISR + B effects play an important role as we demonstrate below. Therefore we will make use of several other useful kinematical variables, such as

- (i) missing transverse momentum, \cancel{E}_T
- (ii) charged lepton energy (muon in particular), E_μ
- (iii) angle of reconstructed W boson in the LAB system, $\cos\theta_W$
- (iv) the energy of W -boson reconstructed from the dijet pair, E_{jj} .

C. The strategy for the signal exploration

It has been shown that the e^+e^- colliders such as ILC and CLIC provide an excellent opportunity for discovery of DM and study its properties for some promising theories, including supersymmetry (see, e.g., Refs. [95,96]). In this paper we also demonstrate that this is the case for the $e^+e^- \rightarrow D^+D^-$ process under study with the signatures discussed above in Sec. III A. The cross section of this process for both DM theories we study here is large enough in comparison with the respective SM background, such that not only DM discovery is possible at ILC and CLIC but also determination of DM properties.

The masses M_+ and M_D can be determined from the edges of the W -boson energy distribution which can be measured using dijets originating from $D^+ \rightarrow DW^\pm \rightarrow Djj$ decay chain as we discuss in Sec. III E 1, (see Refs. [97,98] for MSSM and [51–53] for I2HDM model cases). However, this method provides an accuracy worse than that which can be achieved by using the lepton energy distribution which we exploit in our study, Sec. III E 2, together with the usage of dijet energy. Indeed, the accuracy

of the jet energy resolution is typically 1 order of magnitude worse than muon momentum resolution [99] for ILC, which eventually affects the edges of the respective distributions and consequently the accuracy of the mass measurement. The energy distribution of leptons from the $D^\pm \rightarrow DW^\pm \rightarrow D\ell\nu$ signal has two kink points whose positions are determined by the decay chain kinematics and can be used to determine the M_+ and M_D masses of D^+ and D , respectively. The energy distribution of the W boson (which can be determined from dijet decay channel) also has two kinks which can be used as an important complementary way to measure the masses of DM particles.

We would also like to note that charge lepton and W -boson energy distributions for both—spin zero and spin-half DM cases that we study here—are quite similar as we demonstrate in the following section. However, the angular distributions of W bosons from D^+ decay as well as the signal production cross sections are quite different for spin zero and spin-half DM. These two observables allow one to very clearly distinguish the spin of DM from the signal under study at lepton colliders.

The strategy for DM discovery with the respective signature we discuss here is very different from the case when the lightest charged D -odd particle is charged slepton, the spin-zero superpartner of the SM charged lepton. In this case, the important signal channel is the $e^+e^- \rightarrow \tilde{\ell}^+\tilde{\ell}^- \rightarrow \ell^+\ell^-\chi_0\chi_0$ process. This process has dilepton signature which is quite clean and well identifiable but different from the one we study. Also, the energy of an observable lepton—decay product of slepton—is well measurable *in each individual event*, contrary to our case, when similar product of decay, W , is seen as a dijet or lepton plus neutrino with worse measurable energy in each individual event. Therefore, the approach used in the analysis of slepton production (cf. [100–102]) cannot be applied directly to our study.

D. Cross sections for D^+D^- production

It is convenient use the cross section for the SM process

$$\sigma_0 \equiv \sigma(e^+e^- \rightarrow \gamma \rightarrow \mu^+\mu^-) = 4\pi\alpha^2/3s, \quad (28)$$

which allows us to express the QED cross section of the $e^+e^- \rightarrow D^+D^-$ process with the photon exchange only as

$$\sigma_\gamma = \begin{cases} \sigma_0\beta_D \left[1 + \frac{2M_+^2}{s} \right] & \text{if } s_D = \frac{1}{2}, \\ \sigma_0 \frac{\beta_D^3}{4} & \text{if } s_D = 0 \end{cases}, \quad (29)$$

where $\beta_D = \sqrt{1 - 4M_+^2/s}$. Now we can express the total cross section of the $e^+e^- \rightarrow D^+D^-$ process as

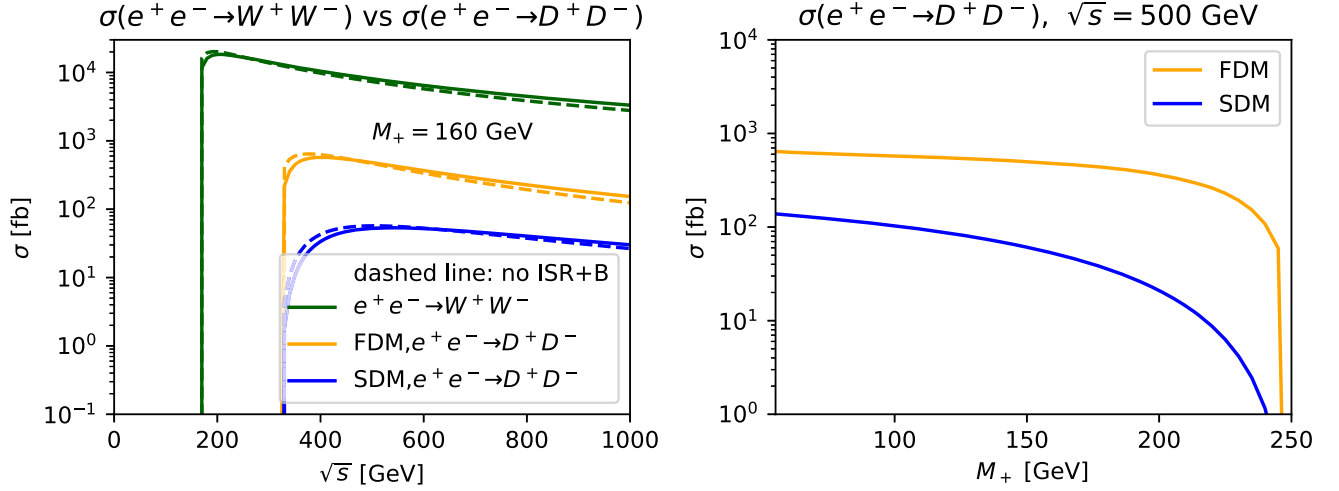


FIG. 1. Left: cross section versus \sqrt{s} for background $e^+e^- \rightarrow W^+W^-$ process (green) compared to the cross section of $e^+e^- \rightarrow D^+D^-$ signal processes for fermion (orange) and scalar (blue) dark matter for BP1 ($M_+ = 160$ GeV). Solid (dashed) lines present results for ISR + B effects switched on (off), respectively. Right: $e^+e^- \rightarrow D^+D^-$ cross section versus M_+ .

$$\sigma = \sigma_\gamma + \sigma_{\gamma/Z} + \sigma_Z = \sigma_\gamma \left[1 + \frac{\kappa_{\gamma/Z}}{1 - \frac{M_Z^2}{s}} + \frac{\kappa_Z}{(1 - \frac{M_Z^2}{s})^2} \right], \quad (30)$$

where $\sigma_{\gamma/Z}$ and σ_Z represent the contribution from the γ/Z interference and squared diagram with Z -boson exchange, respectively. The corresponding $\kappa_{\gamma/Z}$ and κ_Z coefficients are given by

$$\kappa_{\gamma/Z} = \frac{\cos 2\theta_W (2 \cos 2\theta_W - 1)}{4 \cos^2 \theta_W \sin^2 \theta_W} \approx 0.0867, \quad (31)$$

$$\kappa_Z = \frac{\cos^2 2\theta_W (\cos^2 2\theta_W + (\cos 2\theta_W - 1)^2)}{32 \cos^4 \theta_W \sin^4 \theta_W} \approx 0.162. \quad (32)$$

The respective signal cross sections for both models and both benchmarks as well as for the leading SM background $e^+e^- \rightarrow W^+W^-$ are presented in Fig. 1.

For our benchmarks, the $e^+e^- \rightarrow D^+D^-$ cross section for the fermion DM (FDM) case is close to σ_0 , (which makes its use convenient) while for scalar DM (SDM) case the cross section is about 1 order of magnitude lower. The annual integrated luminosity \mathcal{L} for the ILC project [96] is expected to be 500 fb^{-1} which provides of the order 10^5 and 10^4 events for FDM and SDM cases, respectively. The initial ratios of the FDM and SDM signals to the $e^+e^- \rightarrow W^+W^-$ background are about $\frac{1}{10}$ and $\frac{1}{100}$, respectively.

To measure the $e^+e^- \rightarrow D^+D^-$ cross section at the experimental level one should measure the sum over all processes with signatures (21) and (22) [that is about 7/9 of the total cross section of D^+D^- production, since our signature does not include the dilepton final state which is $2 \times (3/9 \times 3/9) = 2/9$]. When masses M_+ is measured, the cross section of $\sigma(e^+e^- \rightarrow D^+D^-)$ process can be

calculated and compared with the measured one. Since the difference between the FDM and SDM signal is about 1 order of magnitude, the knowledge of the cross section would allow us to distinguish DM spin for these two models. One should note, that in case of supersymmetry the FDM cross section can be modified by t -channel diagrams with the sleptons, which could reduce the cross section by about factor of 2, which, however, would still allow us to discriminate FDM from the SDM case.

E. W and charged lepton energy distribution and dark matter mass reconstruction

We proceed with a discussion of the features of the W and charged lepton energy distributions for processes (21) and (22), comprising the positions of discontinuities and end points, expressions for which are derived using simple kinematics.

1. W energy distributions

First we consider the energy distribution of W (which may be virtual) with mass M_W^* . In the regime where W may be produced on-shell (i.e., $M_+ - M_D > M_W$), then $M_W^* = M_W$. However, when W is produced off-shell its maximum effective mass is $M_W^* = M_+ - M_D$ for W^* at zero momentum. In the rest frame of D^\pm we have a two-particle decay $D^\pm \rightarrow DW^\pm$. The energy and three-momentum of the W boson in the D^\pm rest frame (labeled by superscript D) are given by

$$E_W^D(M_W^*) = \frac{M_+^2 + M_W^{*2} - M_D^2}{2M_+},$$

$$p_W^D(M_W^*) = \frac{\sqrt{(M_+^2 - M_W^{*2} - M_D^2)^2 - 4M_D^2 M_W^{*2}}}{2M_+}. \quad (33)$$

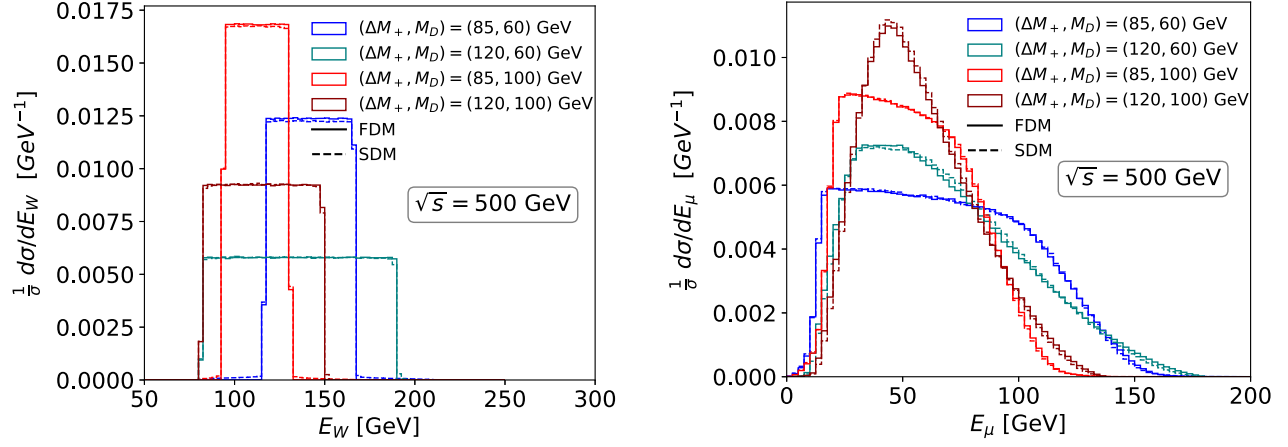


FIG. 2. The energy spectra (without ISR + B) of the W (left) and muon (right) for different DM mass, m_D , and mass split with its charged partner, ΔM_+ . Solid and dashed lines correspond to FDM and SDM, respectively.

Denoting θ as the W^+ escape angle in the D^+ rest frame with respect to the direction of D^+ motion in the laboratory frame, and using $c \equiv \cos \theta$, we find the energy of W^+ in the laboratory frame to be

$$E_W = \gamma_D(E_W^D + c\beta_D p_W^D) \Rightarrow E_W^{(-)}(M_W^*) < E_W < E_W^{(+)}(M_W^*), \quad (34)$$

where

$$E_W^{(\pm)}(M_W^*) = \gamma_D(E_W^D \pm \beta_D p_W^D), \quad (35)$$

with $\gamma_D = \frac{\sqrt{s}}{2M_+}$.

For the on-shell W ($M_W^* = M_W$) case, the kinematical edges of the W energy distribution are

$$E_W^{(\pm)}(M_W) = \frac{E}{2} \left[1 + \frac{M_W^2 - M_D^2}{M_+^2} \pm \frac{\sqrt{(M_+^2 - M_W^2 - M_D^2)^2 - 4M_D^2 M_W^2}}{M_+^2} \right] \times \sqrt{1 - \frac{M_+^2}{E^2}}, \quad (36)$$

where E is the D^\pm energy, which is quite different from delta-function shape of the background distribution, peaking at E in the absence of ISR + B. We show the W -boson energy distribution in Fig. 2 for both the SDM and FDM cases. In reality ISR + B, as we show later, introduces an important smearing which makes the background non-negligible.

For the off-shell case ($M_+ - M_D < M_W$) although these equations hold for events with both a virtual W and real D produced at rest in the D^\pm frame, the kinematic edges are smeared as a result of variation the final state momenta

(and, consequently, the four-momentum of the virtual W) over the phase space. This is demonstrated below in Fig. 5 where the kinematic edges are not clearly visible.

In a well-known approach, one measures edges in the energy distributions of dijets, representing W coming from $D^\pm \rightarrow DW^\pm$ decay [97,98]. However, the individual jet energies and, consequently, effective masses of dijets cannot be measured with a high precision. The observed lower edge of the W energy distribution in the dijet mode is smeared because of this. One can only hope for a sufficiently accurate measurement of the upper edge of the W energy distribution, E_W^+ given by Eq. (36). Therefore we suggest to extract the second quantity for derivation of masses from the lepton energy spectra. The lepton energy is measurable with a higher accuracy in comparison to the dijet one. We will show that the singular points of the energy distribution of the leptons in the final state with signature (22) are kinematically determined, and therefore can be used for a mass measurement.

2. Charged lepton energy distributions in $e^+e^- \rightarrow D^+D^- \rightarrow DDW^+W^- \rightarrow DDq\bar{q}\ell\nu$

We next study the distribution of events over the muon energy, E_μ . The fraction of such events for each separate lepton, e^+ , e^- , μ^+ or μ^- , is about $1/9 \times 2/3 = 2/27 \simeq 0.074$, while their sum is about $4 \times 2/27 \simeq 0.30$ of the total cross section of the process.

In the following sections we consider only muons, so that in the W rest frame and the laboratory system with W energy E_W , respectively, we have

$$E_\mu^W = |\vec{p}_\mu^W| = M_W^*/2, \quad \gamma_W = E_W/M_W^*, \quad \beta_W = \sqrt{1 - \gamma_W^{-2}}. \quad (37)$$

Just as before, we denote θ_1 as the escape angle of μ relative to the direction of the W in the laboratory frame and

use $c_1 = \cos \theta_1$. The muon energy in the laboratory frame is

$$E_\mu = \frac{E_W}{2}(1 + c_1 \beta_W). \quad (38)$$

Muon energies lie between energies $\frac{1}{2}(E_W \pm \sqrt{E_W^2 - M_W^{(*)2}})$. The maximum muon energy, E_μ^{\max} , may be determined from the highest value of W energy, i.e., $E_W = E_W^{(+)}$ from Eq. (36) (see Appendix C 1):

$$E_\mu^{\max} = \frac{E}{2}(1 + \beta_D) \left(1 - \frac{M_D}{M_+}\right). \quad (39)$$

With a shift of E_W from these boundaries inwards, the density of states in the E_μ distribution grows monotonically due to contributions of smaller E_W values up to $E_\mu^{(\pm)}$ values, corresponding to the lowest value of W energy $E_W^{(-)}$ from Eq. (36). At these points the energy distributions of muons have kinks, located at $E_\mu^{(\pm)}$. Between these kinks, the E_μ distribution is approximately flat. The following equation (derived in Appendix C 2),

$$E_\mu^{(\pm)} = \frac{E_W^{(-)} \pm \sqrt{(E_W^{(-)})^2 - M_W^2}}{2}, \quad (40)$$

gives the upper and lower bounds in the muon energy distributions.

At $M_+ - M_D > M_W$, the positions of the upper edge in the dijet energy distribution $E_W^{(+)}$ (36) and the lower kink in the muon energy distribution $E_\mu^{(-)}$ (40) give us two equations necessary for determination of M_D and M_+ (derived in Appendix C 3):

$$M_D^2 = M_W^2 - M_+^2 \left[\frac{1}{E}(\alpha + \beta) - 1 \right], \quad (41)$$

$$M_+^2 = 2 \left[\frac{E^2(\alpha\beta + M_W^2) - \sqrt{E^4(\alpha^2 - M_W^2)(\beta^2 - M_W^2)}}{(\alpha + \beta)^2} \right], \quad (42)$$

where α and β are defined as

$$\alpha = \frac{4E_\mu^{(+2)} + M_W^2}{4E_\mu^{(+)}}, \quad \beta = \frac{4E_\mu^{(-2)} + M_W^2}{4E_\mu^{(-)}}. \quad (43)$$

The position of the upper edge in the dijet energy distribution $E_W^{(+)}$ should be extracted from all events with signatures (21), (22), while the position of the lower kink in the muon energy distribution $E_\mu^{(-)}$ can be extracted from events with signature (22) only.

If a D_2 particle is absent or $M_{D_2} > M_+$, the results (38)–(40) are valid since one can neglect the interference between the signal and SM diagrams as we discuss below. The shape of the energy distribution of leptons (with one peak or two kinks) allows us to determine which case is realized, $M_+ - M_D > M_W$ or $M_+ - M_D < M_W$. The energy distributions (without ISR + B effects) of muons E_μ alongside E_W are presented in Fig. 2 for both the SDM and FDM cases.

While spin does not affect the shape of distributions in Fig. 2, the different DM masses and mass split scenarios can be easily distinguished by using both energy spectra E_W and E_μ . For the W energy distributions in the left plot, increasing ΔM_+ spreads the energy distribution across a larger range. The W is produced nearly at rest when near the $D - D^+$ mass split but can have a larger range when given more energy and is more boosted.

This is opposite in the case of muon energy distributions in the right plot, where increasing ΔM_+ narrows the distributions. When the width of E_W is minimal, this maximizes the width of E_μ because the muon can go exactly along W or opposite this direction, making the muon distribution as wide as possible. If W has larger phase space then it is not aligned along the direction of D^+ . In this case the W energy is not fixed and can be varied, which leaves less phase space to muon for its energy variation.

In the W energy distributions, increasing DM mass shifts the distributions to lower energies. This is also the case for muon energy distributions, as the tails extend to higher energies for smaller DM mass. Since a heavier DM is produced, this takes a larger fraction of the system's energy, giving less energy to the W and muons for the same input energy.

The low and high end kinks can be very close or even overlap either for E_W or E_μ energy distributions, which would eventually spoil M_+ and M_D determination. The key point we stress here is that these kinks *never overlap for both distributions simultaneously*, as is demonstrated in Fig. 3, meaning that M_+ and M_D masses can be always reconstructed. When kinematic edges are not distinguishable in the E_μ energy distribution, the E_W distribution displays a maximal separation of kinematic edges and vice versa. This is an important feature of the signal which highlights the complementary power of the two observables which allows us to effectively extract DM masses in the whole parameter space relevant to the ILC signal under study.

Observation of events with signature (21), (22) will be a clear *signal* for DM particle candidates. The nonobservation of such events will allow us to find lower limits for masses M_+ , like [51–53]. At $M_+ < \frac{\sqrt{s}}{2}$, the cross section $e^+e^- \rightarrow D^+D^-$ is a large fraction of the total cross section of e^+e^- annihilation, making this observation a very realistic task.

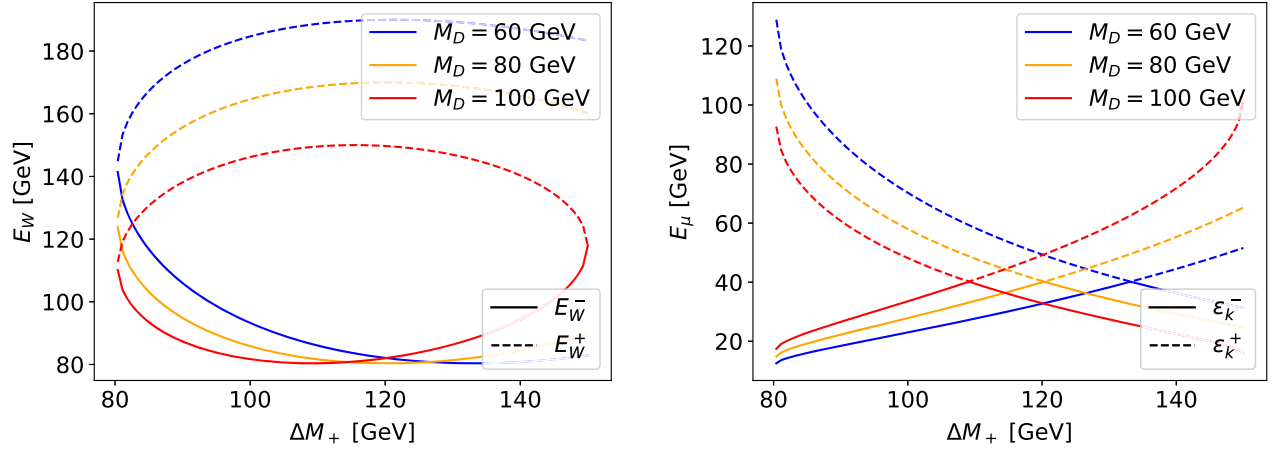


FIG. 3. The dependence of position of kink of the W (left) and muon (right) energy distributions on the DM mass, m_D , and mass split with its charged partner, ΔM_+ . Here solid (dashed) lines correspond to lower (upper) kinks of the respective energy distributions.

3. Distortion of the energy distributions from width effects, ISR + B and intermediate τ 's

A more detailed analysis reveals two main sources of distortion of the energy distributions (we neglected them in our preliminary analysis).

- (1) The final width of W and D^\pm leads to a blurring of the singularities derived. This effect increases with the growth of $M_+ - M_D$.
- (2) The energy spectra under discussion will be smoothed due to QED initial state radiation and beamstrahlung.
- (3) Smearing from intermediate τ leptons in the cascade $D^- \rightarrow DW^- \rightarrow D\tau^- \nu \rightarrow D\mu^- \nu \nu$

For the on-shell W energy distributions with scalar and fermion DM shown in Fig. 4 the upper and lower edges in E_W are clearly visible. However, the ISR + B smearing effect increases the uncertainty in edge identification, especially for the upper edge in E_W . For the off-shell W case, its energy distributions in Fig. 5 shows no visible

kinks or edges, making it impossible to determine DM masses, regardless of ISR + B effects.

The effect of ISR + B which distorts the parton level muon energy distributions is presented in Fig. 6 left and right for SDM and FDM, respectively (for BP1). The blue line corresponds to production of $D^\pm DW^\mp$ and subsequent decay of W boson, i.e., W -width effects are not included. The yellow line corresponds to simulation of the full production cross section, taking into account all widths. This effect smooths $E_\mu^{(+)}$ considerably, but the dominant distortion comes from the effects of ISR + B, as shown by the green line. In CalcHEP, ISR is modeled using the equation by Jadach, Skrzypek, and Ward [103], and bremsstrahlung by that of Chen [104]. The key observation here is that the left-hand kink, $E_\mu^{(-)}$, remains visible.

The process $D^- \rightarrow DW^- \rightarrow D\tau^- \nu \rightarrow D\mu^- \nu \nu$ also modifies the spectra just discussed. The energy distribution of τ produced in the decay $W \rightarrow \tau \nu$ is the same as that for μ or e [within the accuracy of $\sim (M_\tau/M_W^*)^2$]. Once produced,

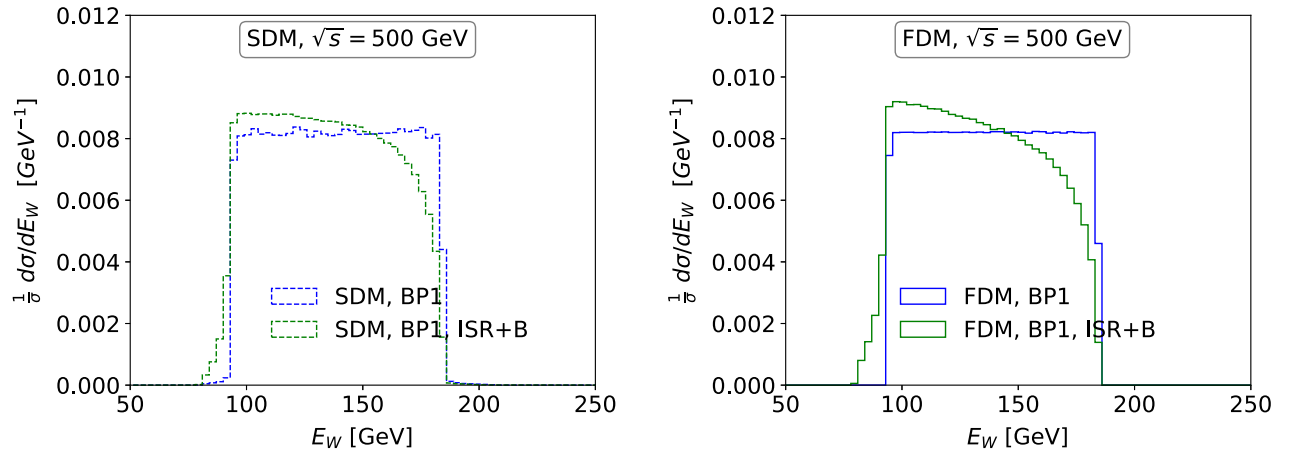


FIG. 4. The W energy distribution for BP1, the on-shell W case, for SDM (left) and FDM (right).

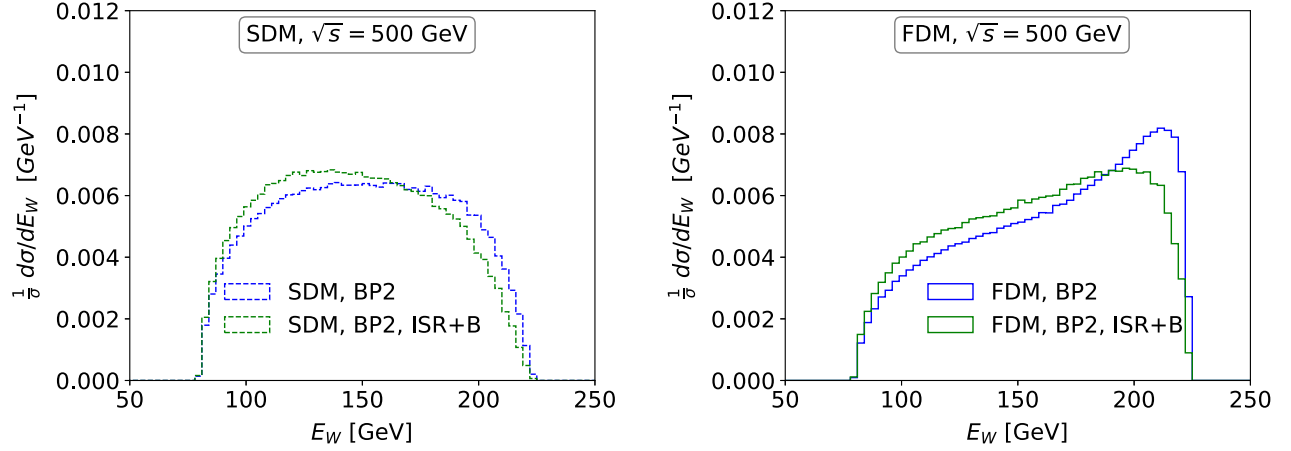


FIG. 5. The W energy distribution for BP2, the off-shell W case, for SDM (left) and FDM (right).

τ decays to $\mu\nu\nu$ in 17% of cases (the same for decay to $e\nu\nu$). These muons are added to those discussed above. In the τ rest frame, the energy of muon is $E_\mu^* = yM_\tau/2$ with $y \leq 1$. The energy spectrum of muons is $dN/dy = 2(3-2y)y^2$. The signal evaluation is presented as energy distributions of muons in the Lab frame. It is clear that this contribution is strongly shifted towards the soft end of the entire muon energy spectrum.

In Fig. 7, we compare the normalized muon energy distributions for SDM and FDM, including all width and ISR + B effects. Since positions of kinks are kinematically determined, it is not surprising that calculations for distinct models (containing different angular dependence) demonstrate variations in shapes, but do not perturb the position of kinks. We see that for FDM, $E_\mu^{(+)}$ is less well preserved than for SDM. Also, the higher energy tail demonstrates small differences in behavior, however does not change the end point, $E_\mu^{(+)}$, required for measurement of mass. This small difference between overall shapes suggests that muon energy is not a good observable to differentiate between spins of DM, but conversely that it is a good observable for

spin-independent measurements of mass. Note that spin correlations were taken into account from $2 \rightarrow 4$ process.

The right plot in Fig. 7 shows the muon energy distribution for the off-shell W decay case. In this case, $E_\mu^{(-)}$ is easily distinguishable between DM spins, including some differences in the shapes of the distribution tails. However, $E_\mu^{(+)}$ does not exist in this case, so one must rely solely on $E_\mu^{(-)}$ for mass and spin determination for the off-shell case. In the next section we discuss the observable that can be used for DM spin determination.

F. Angular distributions for dark matter spin discrimination

We have found that the remarkable observable, which can distinguish the spin of DM, is the angular distribution of W -boson with respect to the electron beam in the lab frame. We found that D^+ angular distribution is determined by the spin of DM (and in the case of s -channel SM vector mediators—photon and Z boson). For spin zero and spin one-half of DM:

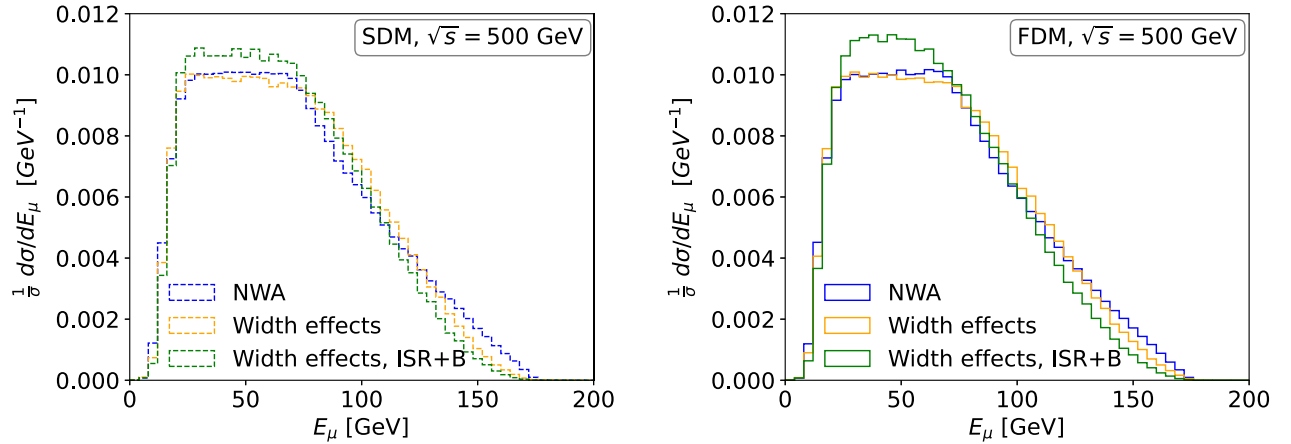


FIG. 6. Muon energy distribution at BP1 for SDM (left) and FDM (right).

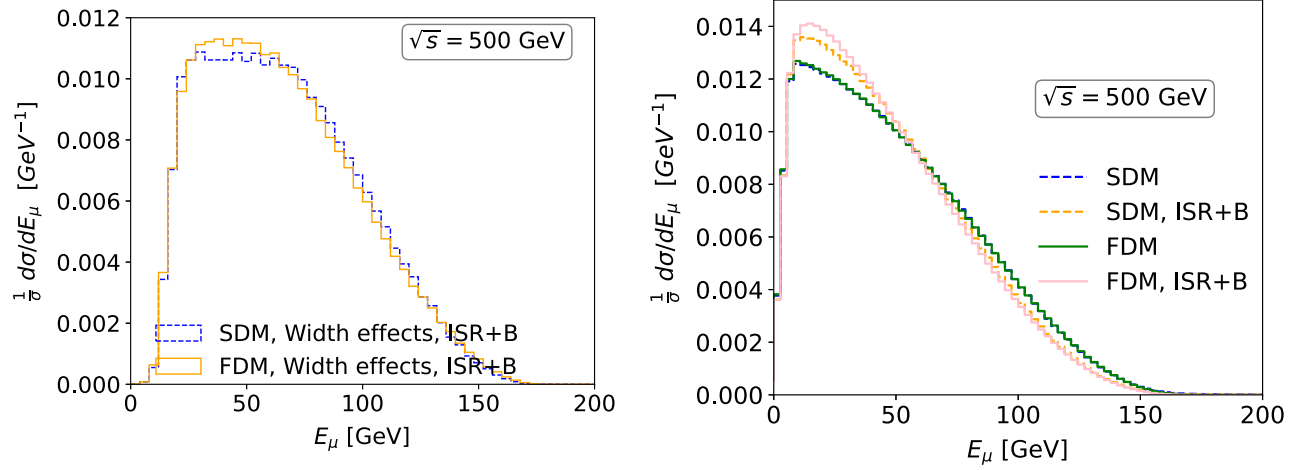


FIG. 7. Comparing SDM and FDM normalized muon energy distributions for BP1 (left) and BP2 (right) values, including width and ISR + B effects.

$$\frac{d\sigma}{d\cos\theta_{D^\pm}} \propto \begin{cases} 1 - \cos^2\theta_{D^\pm}, & \text{for scalar } D^\pm \\ 1 + \frac{s-4M_\pm^2}{s+4M_\pm^2} \cos^2\theta_{D^\pm}, & \text{for fermion } D^\pm. \end{cases} \quad (44)$$

On the other hand, the angular distribution of W boson from D^\pm decay is strongly correlated with the D^\pm one. This can be observed from Fig. 8 (left), where we present normalized angular distributions for D^\pm and W^\pm for two benchmarks of the fermion and scalar DM cases. One can see that the shapes of the D^\pm distributions, given by Eq. (44) determine the angular distribution of its decay product W^\pm , whose angular distribution is very close to its parent, D^\pm . While the (inverted parabolic) shape of D^\pm angular distribution is the same for different masses of DM in case of scalar DM, the shape of angular distribution for the fermion DM case has mild dependence on DM mass and in the extreme case of the D^\pm production at the threshold it becomes flat, but still clearly distinguishable

from the inverted parabolic shape of the angular distribution for the scalar DM case.

The different shapes of the distributions for DM with different spins have a very simple physical explanation. Since the mediator for D^+D^- production is the spin-one SM vector bosons—photons and Z boson, only left-left (LL) or right-right (RR) spin configuration for the initial e^+e^- state is allowed. In the case of scalar DM, the forward-backward scattering of the D^+D^- pair is forbidden, since the forward-backward D^+D^- pair cannot form orbital momentum equal to 1 to match the spin of the mediator. This angular momentum conservation is reflected in $(1 - \cos^2\theta)$ dependence of the angular distribution of the scalar D^\pm particles. At the same time, in the case of fermion DM the forward-backward scattering of D^+D^- with their LL or RR final state spin configuration (matching spin one mediator) is naturally allowed, which is reflected in the $(1 + \frac{s-4M_\pm^2}{s+4M_\pm^2} \cos^2\theta)$ functional

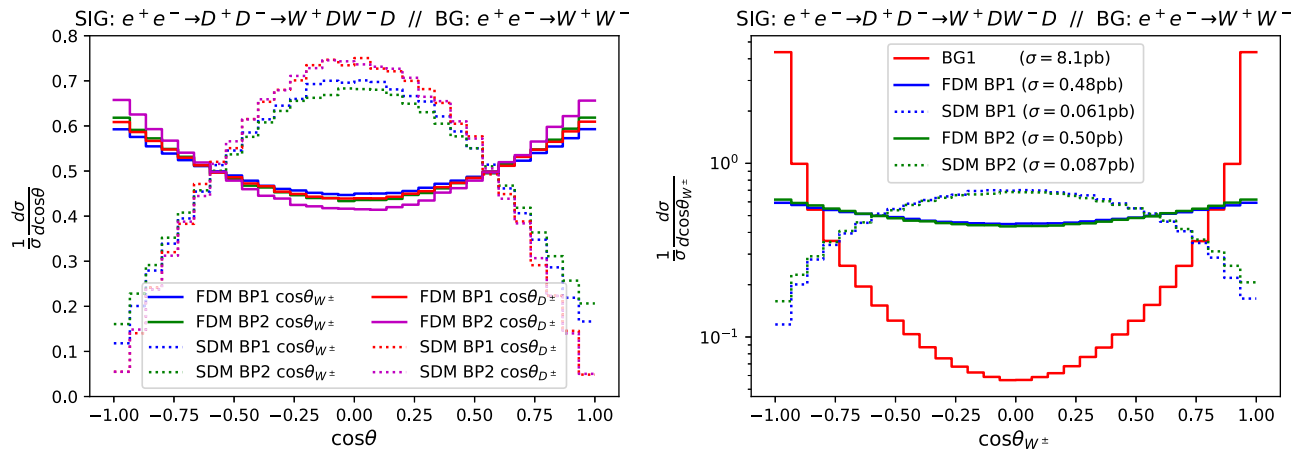


FIG. 8. Left: comparison of the W^\pm and D^\pm angular distributions with respect to beam direction in the lab frame. Right: the angular distribution of W^\pm with respect to beam direction in the lab frame for signal and background processes.

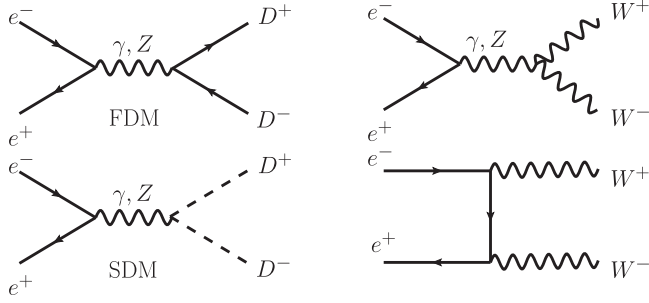


FIG. 9. Signal (left) and background (right) diagrams.

form of the angular distribution of the fermion D^\pm particles.

It is important to stress that angular distributions of W^\pm are very close to D^\pm ones for both on-shell and off-shell W -boson cases. This makes the approach of distinguishing DM with different spins applicable to the whole model parameter space, once the W mboson (on-shell or off-shell) is reconstructed from the dijet.

Another remarkable property of the signal angular distributions for both spin zero and spin one-half DM is that they are very different from the background. This is demonstrated in Fig. 8 (right), where we present normalized angular distributions for W^\pm for both benchmarks from both DM models as well as the leading $e^+e^- \rightarrow W^+W^-$ background. One can see that the background distribution has very pronounced forward-backward peak even in comparison with the distribution for the fermion DM. The reason for this is the t -channel diagram with the electron exchange for the background, shown in Fig. 9 (right) which plays an important role and provides the gauge invariance together with the s -channel γ/Z diagram. This is contrary to the signal case, which has only s -channel γ/Z diagram [Fig. 9 (left)] for the D^+D^- . In the case of an additional t -channel diagram for sleptons production which could take place in case of supersymmetry, the angular D^\pm and, respectively, W^\pm distributions will be still quite different from W^+W^- , as shown in [15].

Therefore, the angular distribution of W^\pm from D^\pm is a very powerful observable to discriminate the spin of DM. Moreover, as we have found in our study, this variable is the generic one for the whole parameter space of a given model and therefore it allows one to successfully distinguish signal models as well as background between each other as we demonstrate below.

IV. SIGNAL VERSUS BACKGROUND ANALYSIS AND DETERMINATION OF DARK MATTER MASS AND SPIN

In this section, we study various background processes and suggest strategies to optimize the statistical significance of the signal as well as the signal to background ratio (which controls the impact of systematic errors).

This analysis uses the kinematical observables and distributions discussed in Sec. III. The ‘‘backgrounds’’ discussed here are of two distinct types:

- (I) SM backgrounds—reducible model-independent backgrounds, which influence observation of the model.
- (II) Model specific irreducible backgrounds—those which can potentially obscure precise measurement of the shape and kinematic features (as presented in Sec. III) of signature (22).

Backgrounds of type-II have the same final state particles as the signal process $e^+e^- \rightarrow D^+D^- \rightarrow W^+W^-DD$. Since the aim of the analysis is to accurately measure the masses of the models and determine the spin of DM, our strategy is to minimize both types of background without significantly distorting the shape of the signal. In this section we perform signal versus background optimization at the fast detector simulation level and present results demonstrating the possibility of mass and spin determination of DM which is the main aim of this paper.

A. Background processes

In this study we focus on the signal process (22) with the respective ‘‘dijet + (e or μ) + \cancel{E}_T ’’ signature. The total cross section for background processes providing this signature is ~ 10 – 100 times more than that of the signal, therefore we explore kinematical distributions and optimize kinematical cuts to maximize signal significance and improve signal to background ratio. There are several backgrounds contributing to this signature which we include in our analysis, such as

- (i) [BG1] The process $e^+e^- \rightarrow W^+W^-$. This is by far the dominant background and is of type-I. The cross section of this process itself is 1 (2) order of magnitude higher than the signal from fermion (scalar) DM, as was discussed earlier and illustrated in Fig. 1. There are several kinematical observables which allow us to suppress BG1, for example,
 - (a) the energy of each dijet for BG1 is $E_{jj} = \frac{\sqrt{s}}{2}$, while for the signal E_{jj} will be below $\frac{\sqrt{s}}{2} - M_D$, so a suitable cut on E_{jj} should strongly suppress BG1. The main obstacles for this cut to work perfectly are the ISR + B effects as well as the effect of the detector energy smearing as we demonstrate below.
 - (b) the missing mass, M_{miss} , is zero for BG1 for the ideal detector and no ISR + B effects. If this would be the case, then $M_{\text{miss}} > 2M_D$ would remove BG1 completely since, for the signal, the minimal value of M_{miss} is $2M_D$. This is not the case, as we know, therefore taking into account ISR + B effects as well as realistic detector resolution is crucial for this study.

One should note, however, that in spite of ISR + B and detector effects, both kinematical variables are very efficient for BG1 suppression.

(ii) [BG2] A type-II background. The process

$$e^+e^- \rightarrow W^- DD^+ \rightarrow W^- W^+ DD, \quad (45)$$

which has just one D^\pm in the intermediate state leads to the same final state as the signal process. To simplify the discussion, we detail the case where $M_{D_2} > M_+$ only (as is the case with the benchmarks analyzed here). The contribution of this process is at least α_W times less than that of the signal process since it is genuine $2 \rightarrow 3$ process. The interference of the BG2 process with the signal is also relatively small since this interference is proportional to the small D^\pm width. The overall contribution of BG2 to the total BG is below 1%.

(iii) [BG3] A type-II background. The process

$$e^+e^- \rightarrow DD_2 \rightarrow DD^+W^- \rightarrow DDW^+W^-, \quad (46)$$

could also contribute to the signature under study. This background is absent if $M_{D_2} < M_+$ or $M_{D_2} + M_D > \sqrt{s}$. If the rate of this process is large enough, it will also be observable via $e^+e^- \rightarrow DDZ$ final state (B2). The cross section $\sigma(e^+e^- \rightarrow DD_2)$ is of the same order as $\sigma(e^+e^- \rightarrow D^+D^-)$ in general but can be suppressed in the case of FDM by the small value of singlet-doublet mixing when $M_{D_2} - M_+$ mass split is small (which is the case of our benchmarks dictated by the DM DD constraints). The kinematics of this background is quite different from the signal: all visible particles follow the D_2 direction and therefore will be mostly in just one hemisphere in contrast to the signal process.

Therefore, the contribution of this background process may be suppressed by application of suitable respective cuts. Moreover, in the case $M_{D_2} < M_+ + M_W$ (the case of our benchmarks) this background comes from genuine $2 \rightarrow 3$ process ($e^+e^- \rightarrow DD^+W^-$) with the intermediate D_2 and therefore it is suppressed by α_W in comparison to the signal under study.

(iv) [BG4] A type-I background. There could be an additional pure SM BG process

$$e^+e^- \rightarrow W^+W^-Z \quad (47)$$

contributing to the signature under study, with large \cancel{E}_T and M_{miss} carried away by neutrinos from Z boson produced in association with W^+W^- pair. The corresponding cross section is suppressed at least by α_W in comparison to BG1.

B. Signal versus background analysis and ILC discovery potential

Here we present the signal versus background analysis and ILC discovery potential for DM at nominal integrated luminosity of 500 fb^{-1} (expected at end of run 1). For our analysis we use tools and setup discussed in Sec. IID.

In Figs. 10–12 we present the key signal and background distributions at fast detector simulation (Delphes) level for M_{miss} , E_{jj} and $\cos\theta_{jj}$ respectively for both benchmarks—BP1(left) and BP2(right).

One can see that missing mass, M_{miss} , given by Eq. (27) has a an expected peak at low values as well as a long tail towards the large values (where the signal “lives”) due to the ISR + B and detector energy smearing effects. These effects are crucial for the correct BG estimation and obviously should be taken into account. In the region of large M_{miss} due to the these effects the dominant BG1 is non-negligible—it is comparable to the FDM signal and

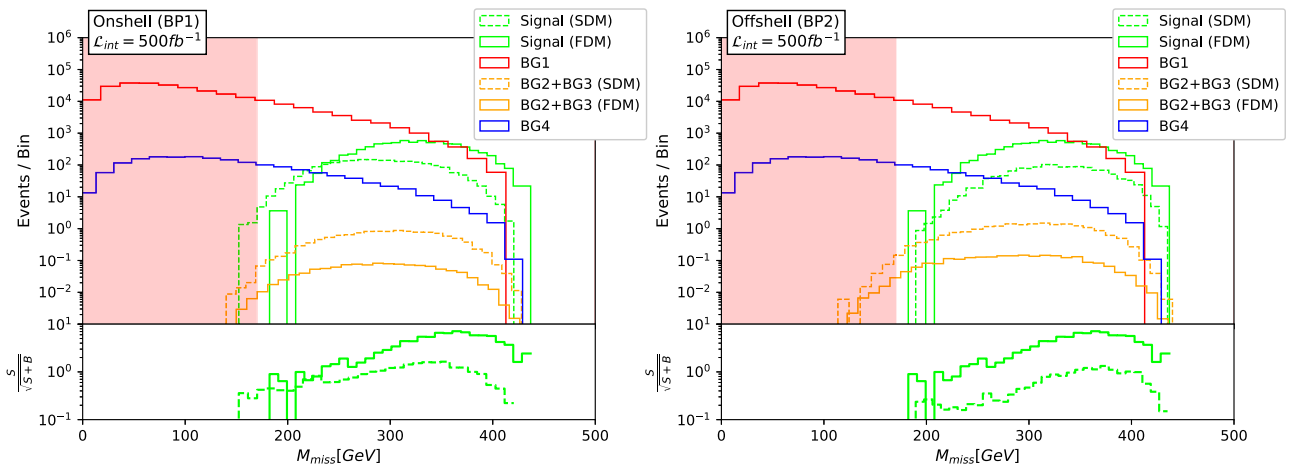
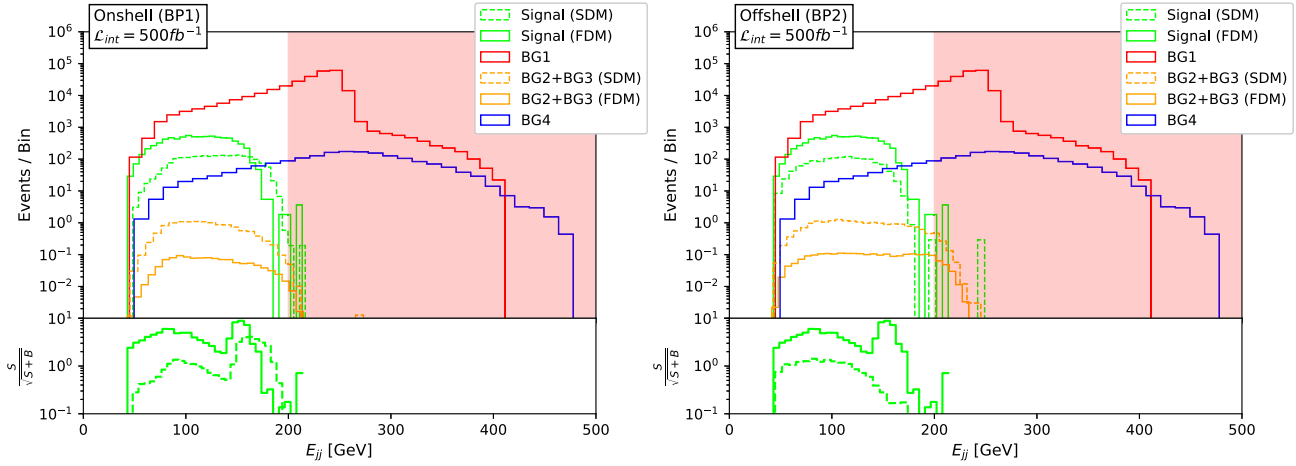


FIG. 10. Missing mass at the detector level for the signal and background processes in both SDM and FDM, for BP1 (left) and BP2 (right).

FIG. 11. Energy of W boson reconstructed from dijet at the detector level.

about 1 order of magnitude above the SDM signal. As we mentioned above without these effects BG1 would be simply a delta function at zero and could be trivially removed. In the low panel of Figs. 10–12 we also present an $S/\sqrt{S+B}$ distribution to give an idea about the statistical signal significance before cuts application.

The dijet energy distribution (Fig. 11) of BG1 and BG4 exhibits a longer tail towards higher values of E_{jj} than the signal, as a result of a t -channel process mediated by an electron neutrino. These are detector level distributions, where we have applied an initial veto requiring at least 2 jets and a single muon. Besides this longer tail, BG1 and BG4 peak at higher values than the signal because these backgrounds do not contain DM pair in the final state. One can see that the difference between the signal and BG1 or BG4 expected at the parton level is preserved also at the detector level. One can also see that the shape of $\cos\theta_{jj}$ distribution (Fig. 12) discussed earlier at the parton level in Sec. III.6 is also preserved at the detector level which brings

an excellent potential to discriminate the DM spin. One should note that model-dependent BG2 + BG3 can be safely neglected even for the case of SDM, for which these backgrounds are 1 order of magnitude higher than for FDM (due to the small singlet-doublet mixing effect in case of FDM).

In the analysis from now on we study “**dijet** + μ + \cancel{E}_T ” signature and quote the respective numbers for the event rates. Based on the properties of the signal and background distributions we propose simple kinematical cuts which are indicated in Figs. 10–12 by red shaded regions. The corresponding cut-flow analyses are presented in Tables II and III. Table II presents details of the evaluation of SM B_I backgrounds and efficiency of the cuts, while Table III presents cut-flow analysis of the signal (S) as well as background B_{II} , which actually becomes part of the signal since it comes from the non-SM diagrams. This table also presents the S/B ratio which is equal to $(S + B_{II})/B_I$ as well as the signal significance

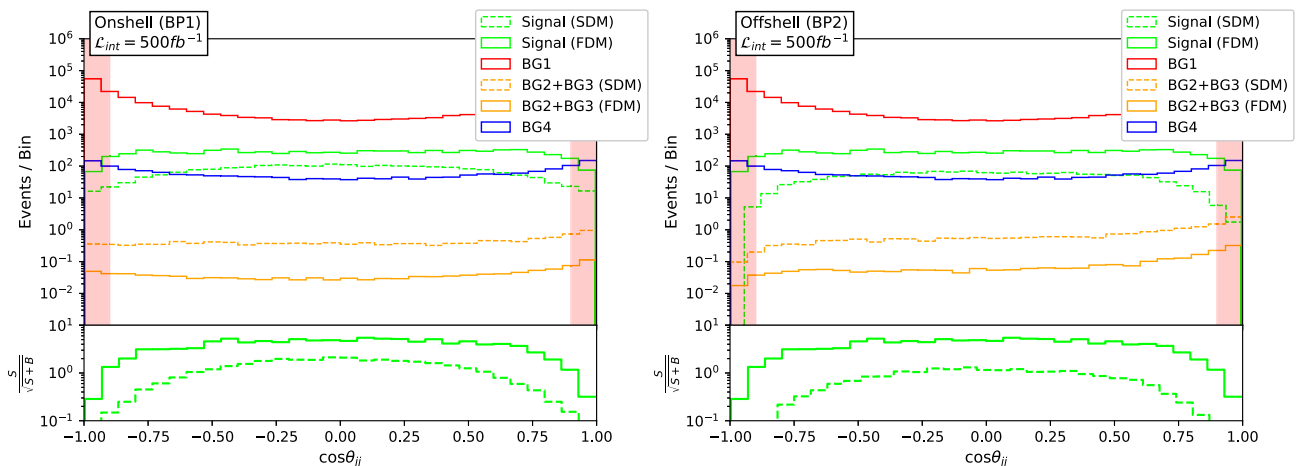
FIG. 12. Scattering angle of W as reconstructed from dijet at the detector level.

TABLE II. Cut flow for the SM BG (BG1 and BG4), which are BP independent.

SM BG cut flow				
Cut	BG1	BG4	B_I	ε_{B_I}
Parton level	6.600×10^5	1.947×10^4	6.795×10^5	...
Reco level	2.921×10^5	1.842×10^3	2.939×10^5	0.433
$M_{\text{miss}} > 170$	4.053×10^4	4.881×10^2	4.101×10^4	0.140
$E_{jj} < 200$	3.718×10^4	2.993×10^2	3.748×10^4	0.914
$ \cos \theta_{jj} < 0.9$	1.902×10^4	2.332×10^2	1.925×10^4	0.514
$ \cos \theta_\mu < 0.9$	1.456×10^4	1.981×10^2	1.476×10^4	0.767

$$\alpha(\delta_{\text{sys}}) = \frac{S}{\sqrt{S+B} + \delta_{\text{sys}}(S+B)}, \quad (48)$$

which includes statistical and systematic uncertainty of the signal. The numbers are presented for the 500 fb^{-1} integrated luminosity and for two values of systematic uncertainty, $\delta_{\text{sys}} = 0$ and $\delta_{\text{sys}} = 0.01$. The starting point of Tables II and III is the reconstruction level (Reco level) after Delphes simulation for which require at least two jets with $p_T^j > 20 \text{ GeV}$ and one muon with $p_T^\mu > 20 \text{ GeV}$. In this example of the cut-flow analysis we apply a simple set of cuts, which demonstrate that cuts on M_{miss} , E_{jj} , $\cos \theta_{jj}$, and $\cos \theta_\mu$ can be chosen such that their cumulative

efficiency will be as high as about 90% for the signal and only about 5%–7% for the background. This is demonstrated in Tables II and III where we present the relative efficiency of each cut after the consequent application one cut after another (see columns ε_S and ε_{B_I} for signal and background, respectively), so their cumulative efficiency is equal to their product.

One should also note that the efficiency of the initial (precut) signal selection is about factor of 2 higher for BP1 in comparison to BP2. This is because the jets and muon from the off-shell W -boson decay in case of BP2 are eventually softer in comparison to the on-shell W -boson decay, so the respective efficiencies for jet reconstruction and muon identification with $p_T > 20 \text{ GeV}$ are, respectively, lower for the BP2.

The kinematical cuts on the key kinematical variables listed in Tables II and III can be further optimized using various techniques, including multivariate cuts analysis, boosted decision trees analysis, or even neural net analysis at a more sophisticated level. However, as one can see, we can achieve high enough significance even without a sophisticated set of cuts and therefore limit ourselves for this study by analysis based on simple cuts on key variables we have found.

In Table IV we present the luminosity required to observe the “**dijet** + μ + \cancel{E}_T ” signature from SDM and

 TABLE III. Cut flow for BP1 (top) and BP2 (bottom) with efficiency and significances, $\alpha(\delta_{\text{sys}})$ for the 500 fb^{-1} integrated luminosity. See details in the text.

BP1 cut flow														
Cut	SDM					FDM								
	S	ε_S	B_{II}	$\varepsilon_{B_{II}}$	$\frac{(S+B_{II})}{B_I}$	$\alpha(\delta_{\text{sys}})$		S	ε_S	B_{II}	$\varepsilon_{B_{II}}$	$\frac{(S+B_{II})}{B_I}$	$\alpha(\delta_{\text{sys}})$	
						$\alpha(0)$	$\alpha(0.01)$						$\alpha(0)$	$\alpha(0.01)$
Parton level	4.519×10^3	...	16.55	...	0.007	5.464	0.589	3.556×10^4	...	1.540	...	0.052	42.06	4.448
Reco level	2.185×10^3	0.484	12.56	0.759	0.007	4.016	0.623	1.848×10^4	0.520	1.185	0.769	0.063	33.06	5.017
$M_{\text{miss}} > 170$	2.182×10^3	0.999	12.52	0.996	0.054	10.50	3.411	1.845×10^4	0.999	1.174	0.991	0.450	75.67	22.01
$E_{jj} < 200$	2.182×10^3	1.000	12.49	0.998	0.059	10.96	3.663	1.844×10^4	1.000	1.168	0.994	0.492	78.00	23.18
$ \cos \theta_{jj} < 0.9$	2.132×10^3	0.977	10.64	0.852	0.111	14.58	5.921	1.651×10^4	0.895	0.946	0.810	0.858	87.30	30.20
$ \cos \theta_\mu < 0.9$	2.027×10^3	0.951	9.587	0.901	0.138	15.65	6.816	1.542×10^4	0.934	0.851	0.899	1.045	88.77	32.43

BP2 cut flow														
Cut	SDM					FDM								
	S	ε_S	B_{II}	$\varepsilon_{B_{II}}$	$\frac{(S+B_{II})}{B_I}$	$\alpha(\delta_{\text{sys}})$		S	ε_S	B_{II}	$\varepsilon_{B_{II}}$	$\frac{(S+B_{II})}{B_I}$	$\alpha(\delta_{\text{sys}})$	
						$\alpha(0)$	$\alpha(0.01)$						$\alpha(0)$	$\alpha(0.01)$
Parton level	4.519×10^3	...	16.55	...	0.007	5.464	0.589	3.556×10^4	...	1.540	...	0.052	42.06	4.448
Reco level	1.352×10^3	0.299	19.98	1.207	0.005	2.487	0.387	7.894×10^3	0.222	2.376	1.543	0.027	14.37	2.213
$M_{\text{miss}} > 170$	1.352×10^3	1.000	19.81	0.992	0.033	6.566	2.147	7.894×10^3	1.000	2.328	0.979	0.193	35.70	11.11
$E_{jj} < 200$	1.351×10^3	1.000	19.18	0.968	0.037	6.858	2.309	7.891×10^3	1.000	2.194	0.943	0.211	37.05	11.84
$ \cos \theta_{jj} < 0.9$	1.345×10^3	0.995	15.85	0.826	0.071	9.369	3.848	7.616×10^3	0.965	1.761	0.802	0.396	46.46	17.61
$ \cos \theta_\mu < 0.9$	1.308×10^3	0.973	14.71	0.928	0.090	10.32	4.551	7.262×10^3	0.954	1.614	0.917	0.492	48.94	19.70

TABLE IV. Table demonstrating the expected luminosity (in fb^{-1}) required to observe a 5σ excess above SM backgrounds.

		Luminosity required for discovery (at 5σ)/ fb^{-1}	
		$\alpha(0)$	$\alpha(0.01)$
SDM	BP1	51.1	149
	BP2	117	789
FDM	BP1	1.59	1.95
	BP2	5.21	7.25

FDM models at the 5σ level for zero and 1% systematic error values, denoted by $\alpha(0)$ and $\alpha(0.01)$ values. We use the cut flow from Tables II and III. The luminosity is calculated using the Asimov dataset, and as such represents an “expected” luminosity for discovery. The number of signal and background events for the respective luminosities is large enough to assume the statistical distribution is approximately Gaussian.

In Fig. 13 we present the luminosity required for discovery as the function of the value of the systematic error using formula (48) for α . From this plot, we see that if systematic errors are above a few percent, then discovery of the SDM benchmarks via the channel under study alone at ILC is problematic for simple cut-based analysis we use here. However, various studies at future e^+e^- colliders [105,106] including ILC shows that the control of the systematic error for the leading W^+W^- background at the 1% level is quite realistic.

One should also add that the background can be further controlled and reduced using electron-positron beam polarization. We have checked that, for example, in the case of 80% polarization of both electron (right) and positron (left) beams the background is reduced by about

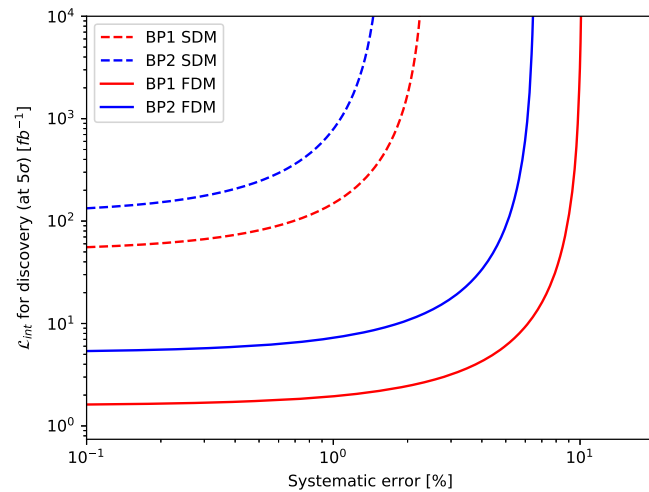


FIG. 13. Luminosity required for a 5σ DM signal excess above SM backgrounds as a function of the systematic error percentage based on $\alpha(\delta_{\text{sys}})$ given by Eq. (48).

factor of 20 while the signal from both models drops down by less than a factor of 2 only.

C. DM mass determination

1. Kinematic fitting

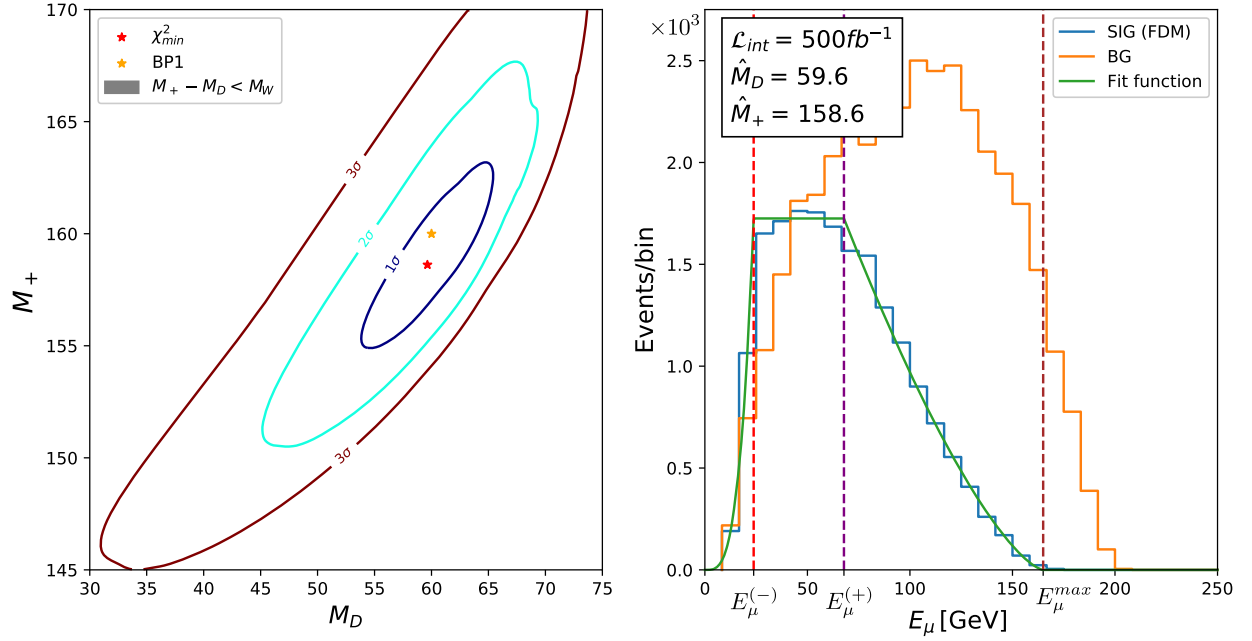
In our analysis we approximate shape of the muon energy distribution using a piecewise function. The functional form has power-law dependence for the tail regions, and a constant for the plateau region between the two kinks, described by the following function:

$$f(E_\mu) = \begin{cases} b \left(\frac{E_\mu}{E_\mu^{(-)}} \right)^a & \text{if } E_\mu \leq E_\mu^{(-)} \\ b & \text{if } E_\mu^{(-)} < E_\mu < E_\mu^{(+)} \\ b \left(1 - \frac{E_\mu - E_\mu^{(+)}}{E_\mu^{\text{max}} - E_\mu^{(+)}} \right)^c & \text{if } E_\mu^{(+)} \leq E_\mu < E_\mu^{\text{max}} \\ 0 & \text{if } E_\mu \geq E_\mu^{\text{max}}, \end{cases} \quad (49)$$

where $E_\mu^{(-)}$ and $E_\mu^{(+)}$ are positions of the left and right kinks of the muon energy distribution, respectively. The fit of the muon energy distribution for BP1 using the function (49) was made for the expected number of events, simulated at the Delphes level for each model. We have generated the pseudo-experimental dataset neglecting theory errors. This dataset corresponds to the expected number of events in each bin from a large MC sample (often called the *Asimov dataset*), allowing us to evaluate the expected resolutions for D and D^+ masses. The discrepancy between the piecewise function (49) and the detector level distributions for each model results in a bias on the estimator. To capture this we include a methodological error (conservatively set to be 10% of signal for each bin). We have found that this value of the methodological error gives the result consistent with the input mass and the error from χ^2 profile.

The number of signal + background events is evaluated for realistic statistics, corresponding to the cross section times luminosity for each process. Cuts outlined in Table III are applied, except the cut on $\cos \theta_{jj}$ since this cut smears $E_\mu^{(-)}$ considerably, while other cuts give approximately uniform modulation of the signal distribution. The profile χ^2 is calculated by minimizing over nuisance parameters a , b , and c as well as M_D and M_+ masses expressed via $E_\mu^{(-)}$, E_μ^{max} values of the fit. The mean collision energy after ISR + B was found to be 477.78 GeV from the simulation. This value was used in the fit. As a result, we have found the minimum of this profiled χ^2 , corresponding to the global minimum of the fit, where M_D , M_+ are also allowed to vary.

The result of this fit is illustrated in Figs. 14 and 15 for FDM (500 fb^{-1}) and SDM (20 ab^{-1}) cases, respectively. The right panels of these figures present E_μ distributions for signal and background as well as piecewise functions (49)


 FIG. 14. Profile χ^2 value for kinematic fitting of BP1 (left) and muon energy distribution with best fit (right), for FDM.

determined from the fit together with the $E_\mu^{(-)}, E_\mu^{(+)}$ parameters which have determined the values of M_D and M_+ . The left panels of the Figs. 14 and 15 present the 1-2-3- σ contours in M_D - M_+ plane from the likelihood variation at the respective confidence levels which allows us to determine the errors on the M_D and M_+ masses. Although this shape fitting procedure is less sensitive than template fitting (which we discuss in the next section for BP2 case), it has the key advantage of being model

independent. The example of the numerical output of the fit is given in Table V, which presents the values of the M_D and M_+ determined from the fit as well as the accuracy of their measurement. From this table one can see that the input values of M_D and M_+ —60 and 160 GeV respectively—are consistent with the fit and its accuracy, which is a good cross check of the approach we are using. One can also observe that the accuracy of the FDM mass determination at $500 fb^{-1}$ is similar to that of the SDM at

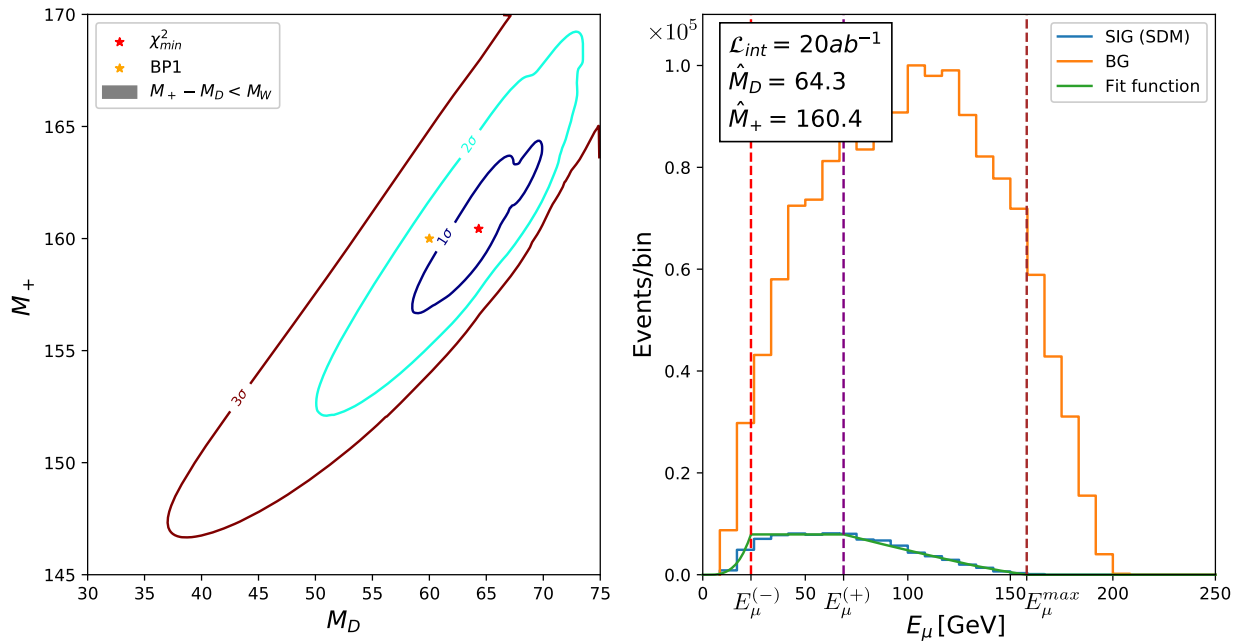

 FIG. 15. Profile χ^2 value for kinematic fitting of BP1 (left) and muon energy distribution with best fit (right), for SDM.

TABLE V. Mass resolutions for BP1 kinematic fitting procedure.

		500 fb ⁻¹	20 ab ⁻¹
FDM	M_D	58.4 ^{+5.7} _{-6.0}	57.6 ^{+1.9} _{-2.2}
	M_+	158.1 ^{+4.0} _{-3.7}	157.4 ^{+2.7} _{-2.4}
SDM	M_D	66.0 ^{+19.2} _{-64.3}	64.3 ^{+3.2} _{-6.1}
	M_+	161.3 ^{+14.7} _{-52.8}	161.0 ^{+3.3} _{-3.9}

20 ab⁻¹. The determination of SDM masses at 500 fb⁻¹ is quite problematic using the simple set of cuts and piecewise function fitting method which requires approximately 40 times more luminosity to obtain comparable precision for SDM as for FDM model.

2. Template fitting

For off-shell W bosons in case of “**dijet** + μ + \cancel{E}_T ” signature for BP2, there are no longer clear kinematic edges

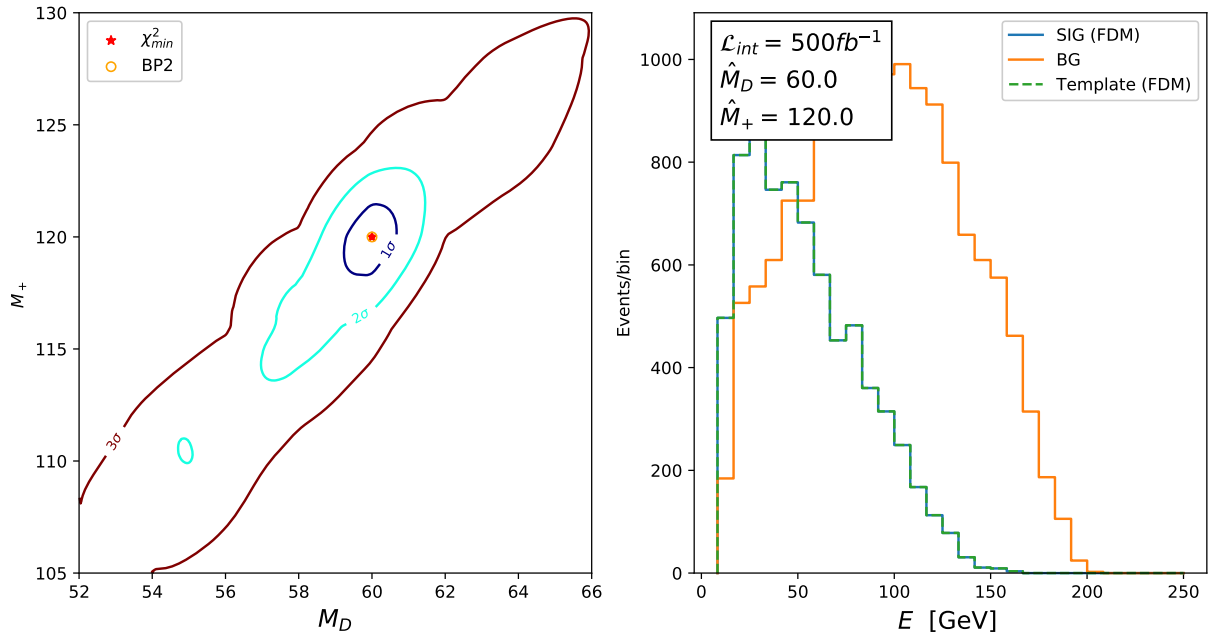
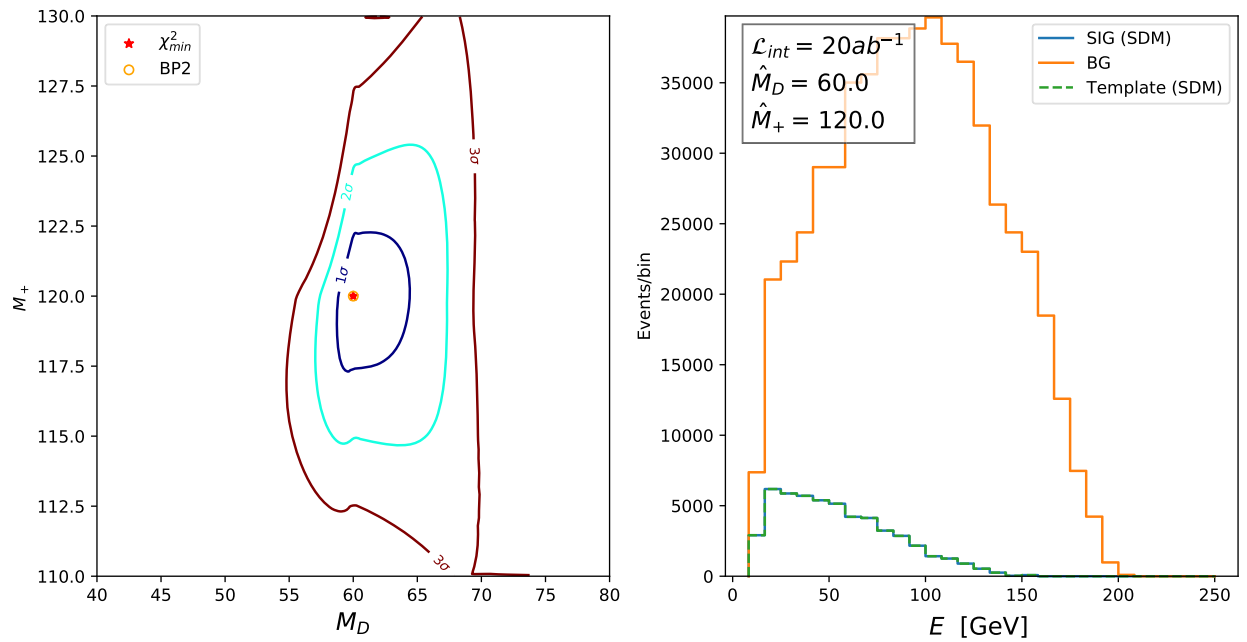
FIG. 16. Profile χ^2 value for template fitting of BP2 (left) and muon energy distribution with best fit (right), for FDM.FIG. 17. Profile χ^2 value for template fitting of BP2 (left) and muon energy distribution with best fit (right), for SDM.

TABLE VI. Mass resolutions for BP2 shape fitting procedure.

		500 fb ⁻¹	20 ab ⁻¹
FDM	M_D	60.0 ^{+0.7} _{-0.8}	60.0 ^{+0.1} _{-0.1}
	M_+	120.0 ^{+1.5} _{-1.7}	120.0 ^{+0.2} _{-0.3}
SDM	M_D	60.0 ^{+24.1} _{-19.7}	60.0 ^{+4.4} _{-1.3}
	M_+	120.0 ^{+22.3} _{-45.9}	120.0 ^{+2.3} _{-2.7}

in E_μ distribution. Therefore, in this case we have employed the Monte Carlo template fitting method. We have produced a 13×13 grid of muon energy distributions for $M_D = 168.0\text{--}170.0$ and $M_+ = 118.0\text{--}122.0$ GeV ranges. Then, using a 2D linear interpolation in (M_D, M_+) space we have calculated the χ^2 contour presented in Figs. 16 and 17 together with the result of the fit. Although this strategy yields better accuracy, information about the overall normalization of the distributions—the cross section—was used, making this approach more model dependent. Indeed, from Table VI which presents details of the template fit of BP2 parameters, one can see this method provides an order of magnitude better accuracy in the case of FDM in comparison to the BP1 piecewise function fit. At the same time, the template fit of BP2 parameters in the case of SDM provides similar accuracy to that of the BP1 piecewise function fit. The reason for this is quite simple: when using the template fit, we do not assume 10% methodological error contrary to the case of piecewise function fit. In case of FDM this error is dominant, that is why, template fit which does not have such an uncertainty improved the accuracy of the mass measurement of the fermion DM. At the same time in the case of SDM, because of its lower signal, the statistical uncertainty is comparable to the methodological error and therefore when we exclude the later one in template fit, we do not achieve a big effect on improving of the accuracy of the mass measurement.

D. Spin discrimination

As discussed in Sec. III F the angular distribution of the W boson reconstructed from dijet is a very important observable to distinguish scalar and fermionic DM as well as to distinguish the signal from the background.

We have performed a binned composite likelihood analysis to estimate discriminating power of these distributions from Fig. 12, assuming that a signal of one model is present. We assume that the mass of the DM is precisely known, noting that more complete treatment would involve a simultaneous fit of mass and spin. Events have been generated for the model assigned to “assumed nature” in Table VII, before the statistical comparison with the alternative model is conducted. We perform the analysis for two cases: using only the shape (signal strength becomes a nuisance parameter μ , which may vary to maximize the likelihood) and also using the signal strength

TABLE VII. Integrated luminosity required to discriminate between spin of DM within these models using binned composite likelihoods.

Assumed nature	\mathcal{L}_{int} to differentiate at 95% CL/fb ⁻¹			
	Shape only		Shape and cross section	
	SDM	FDM	SDM	FDM
BP1	9.8×10^2	30	1.9	3.4
BP2	2.3×10^3	1.2×10^2	9.6	13

predicted by the specific model (in which case $\mu = 1$). In Table VII we present the luminosity required to exclude a given hypothesis at the expected 95% confidence level. Distributions used in this analysis were taken after the M_{miss} and E_{jj} cuts of Table III only. From Table VII one can see first that if one would use the information about the signal cross section, one can discriminate the spin of DM with integrated luminosity of the order of 10 fb^{-1} only. However this discrimination is quite model dependent. On the other hand, even if we do not use the signal cross section as a discriminator, one can still distinguish FDM from SDM scenarios with about 2 ab^{-1} total integrated luminosity in the worst case scenario of the assumed nature model for BP1 or BP2. This discrimination is purely based on the shape of the $\cos \theta_{jj}$ distribution, demonstrating its important power.

V. CONCLUSIONS

In this study we explore the potential of the e^+e^- colliders to discover and determine the properties of DM, such as mass and the spin. The results of this study are applicable for future e^+e^- colliders such as ILC or FCC-ee.

We study two cases of minimal models with DM, D of spin zero and spin one-half, which belongs to the $SU(2)$ weak doublet with the hypercharge $1/2$ and therefore has the charged doublet partner, D^+ . For the case of scalar DM we chose the inert doublet model, while for the case of fermion DM we suggest the new minimal fermion dark matter (MFDM) model with only three parameters. In this MFDM model the $SU(2)$ DM weak doublet interacts with the singlet Majorana fermion and the SM Higgs doublet. In comparison to the previously studied doublet-singlet model with different left- and right-handed interactions of Higgs, DM doublet, and the singlet, MFDM has these couplings equal to each other and this structure is preserved against the quantum corrections.

We suggest two benchmarks for the models under study which provide the correct amount of observed DM relic density and satisfy the current DM direct (and indirect) detection as well as LHC constraints. We also provide the values of oblique S , T , U parameters which are consistent with the current electroweak precision tests. For the case of

MFDM this result is new—we have evaluated formulas for S , T , and U parameters and found that for this model the values of T and U are zero because of the model’s structure, while the values of the S parameter are very close to the SM one.

We chose the particular process $e^+e^- \rightarrow D^+D^- \rightarrow DDW^+W^- \rightarrow DD(q\bar{q})(\mu^\pm\nu)$ providing the signature “**dijet** + μ + \cancel{E}_T ” at 500 GeV ILC collider and study it at the level of the fast detector simulation, taking into account bremsstrahlung and ISR effects. As a result, we have found several key kinematical characteristics that allow us to optimize the signal to background ratio, and discover and identify properties of DM properties. Among them are the missing mass, M_{miss} , the muon energy E_μ , and the angular distribution of the W boson, reconstructed from dijet, $\cos\theta_{jj}$.

In particular, we have shown that E_μ distribution in the case of on-shell W -boson from $D^+ \rightarrow DW^+$ decay (BP1), has characteristic points (kinks), whose positions are kinematically determined by masses of D^+ and D . The successful determination of these points allows us to precisely determine these masses as we have demonstrated using the piecewise function fitting procedure which we suggest in this paper. For the model parameter space with off-shell W -boson (BP2) we have demonstrated the success of the template fit of E_μ distribution, since it does not have kinks in this case. In particular we have demonstrated that in case of fermion DM, the masses can be measured with few percent accuracy already at 500 fb $^{-1}$ integrated luminosity. At the same time, the scalar DM model which has about an order of magnitude lower signal, requires about factor of 40 higher luminosity to reach the same accuracy in the mass measurement. One should also add that the background can be further controlled and reduced using electron-positron beam polarization. We have also found the background can be further strongly suppressed by using the electron-positron beam (right-left) polarization which only mildly affects the signal rate.

We have also found that $\cos\theta_{jj}$ distribution is crucial for the determination of the DM spin. To the best of our knowledge, we have shown for the first time that it allows

to distinguish fermion and scalar DM scenarios with about 2 ab $^{-1}$ total integrated luminosity or less without using the information on BP1 or BP2 cross sections. This discrimination is purely based on the shape of the $\cos\theta_{jj}$ distribution, demonstrating its important role.

The methods of the identification of DM properties we suggest here are generic for the models where DM and its partner belong to the weak multiplet and can be applied to explore various DM models at future e^+e^- colliders such as ILC, CLIC, and FCC-ee.

ACKNOWLEDGMENTS

This work was supported in part by Grants RFBR and NSH-3802.2012.2, Program of Dept. of Phys. Sc. RAS and SB RAS “Studies of Higgs boson and exotic particles at LHC” and Polish Ministry of Science and Higher Education Grant N202 230337. I. G. is thankful to A. Bondar, E. Boos, A. Gladyshev, A. Grozin, S. Eidelman, I. Ivanov, D. Ivanov, D. Kazakov, J. Kalinowski, K. Kanishev, P. Krachkov, and V. Serbo for discussions. We would like to thank Tristan Hosken for his contribution on the very early stage of this study. We acknowledge the use of the IRIDIS High Performance Computing Facility, and associated support services at the University of Southampton to complete this work. A. B. and D. L. acknowledge support from the STFC Grant No. ST/L000296/1 and Soton-FAPESP grant. The work of A. P. was carried out within the scientific program “Particle Physics and Cosmology” of the Russian National Center for Physics and Mathematics.

APPENDIX A: EVALUATION OF THE S AND T PARAMETERS FOR MFDM

To find the contribution of new physics to the oblique parameters one should evaluate quantum corrections to the masses of vector bosons and their mixings, $\Pi_{ZZ}(p^2)$, $\Pi_{Z\gamma}(p^2)$, $\Pi_{\gamma\gamma}(p^2)$, and $\Pi_{WW}(p^2)$ (or in unbroken gauge basis, 3,0 labels refer to W^3 , B gauge bosons, respectively), defined by the effective Lagrangian

$$\mathcal{L}_{\text{oblique}} = \frac{1}{2}Z_\mu\Pi_{ZZ}(p^2)Z^\mu + \frac{1}{2}\gamma_\mu\Pi_{\gamma\gamma}(p^2)\gamma^\mu + Z_\mu\Pi_{Z\gamma}(p^2)\gamma^\mu + W_\mu^+\Pi_{WW}(p^2)W^{-\mu}, \quad (\text{A1})$$

where vacuum polarization functions Π ’s can be expanded in powers of p^2 :

$$\Pi(p^2) = \Pi(0) + p^2\Pi'(0) + \frac{(p^2)^2}{2}\Pi''(0) + \dots, \quad (\text{A2})$$

since the new physics scale is expected to be high. As for I2HDM, for MFDM we are evaluating here S , T , and U observables [86] among the complete set of seven oblique parameters [107] which are related to Π functions as follows:

$$S \equiv \frac{4c_W^2s_W^2}{\alpha} \left[\Pi'_{ZZ}(0) - \frac{c_W^2 - s_W^2}{c_W s_W} \Pi'_{Z\gamma}(0) - \Pi'_{\gamma\gamma}(0) \right] = \frac{4s_W^2 g}{\alpha g'} \Pi'_{30}(0), \quad (\text{A3})$$

$$T \equiv \frac{1}{\alpha} \left[\frac{\Pi_{WW}(0)}{M_W^2} - \frac{\Pi_{ZZ}(0)}{M_Z^2} \right] = \frac{1}{\alpha} \frac{\Pi_{33}(0) - \Pi_{WW}(0)}{M_W^2}, \quad (\text{A4})$$

$$U \equiv \frac{4s_W^2}{\alpha} \left[\Pi'_{WW}(0) - \frac{c_W}{s_W} \Pi'_{Z\gamma}(0) - \Pi'_{\gamma\gamma}(0) \right] - S = \frac{4s_W^2}{\alpha} [\Pi'_{WW}(0) - \Pi'_{33}(0)], \quad (\text{A5})$$

where $\alpha = \alpha_{em}(M_Z)$. In the following expressions we adopt $\Pi^{(\prime)}(0) \equiv \Pi^{(\prime)}$ notation, i.e., omit (0) argument of $\Pi^{(\prime)}$ functions,

To find S , T , and U values we have calculated Π functions for the interaction Lagrangian of the general form:

$$\mathcal{L}_{V\psi\psi} = \bar{\psi}_1 (g_V \gamma^\mu - g_A \gamma^\mu \gamma^5) \psi_2 V_\mu + \text{H.c.} \quad (\text{A6})$$

using dimensional regularization. We have found that

$$\Pi^{(\prime)} = \frac{1}{4\pi^2} ((g_V^2 + g_A^2) \Pi_{V+A}^{(\prime)} + (g_V^2 - g_A^2) \Pi_{V-A}^{(\prime)}), \quad (\text{A7})$$

with $\Pi_{V\pm A}^{(\prime)}$ given by

$$\Pi_{V+A} = -\frac{1}{2} (m_1^2 + m_2^2) (\text{div} + L) - \frac{1}{4} (m_1^2 + m_2^2) - \frac{(m_1^4 + m_2^4)}{4(m_1^2 - m_2^2)} \ln \left(\frac{m_2^2}{m_1^2} \right), \quad (\text{A8})$$

$$\Pi_{V-A} = m_1 m_2 \left(\text{div} + L + 1 + \frac{(m_1^2 + m_2^2)}{2(m_1^2 - m_2^2)} \ln \left(\frac{m_2^2}{m_1^2} \right) \right), \quad (\text{A9})$$

$$\Pi'_{V+A} = \left(\frac{1}{3} \text{div} + \frac{1}{3} L \right) + \frac{m_1^4 - 8m_1^2 m_2^2 + m_2^4}{9(m_1^2 - m_2^2)^2} + \frac{(m_1^2 + m_2^2)(m_1^4 - 4m_1^2 m_2^2 + m_2^4)}{6(m_1^2 - m_2^2)^3} \ln \left(\frac{m_2^2}{m_1^2} \right), \quad (\text{A10})$$

$$\Pi'_{V-A} = m_1 m_2 \left(\frac{(m_1^2 + m_2^2)}{2(m_1^2 - m_2^2)^2} + \frac{m_1^2 m_2^2}{(m_1^2 - m_2^2)^3} \ln \left(\frac{m_2^2}{m_1^2} \right) \right), \quad (\text{A11})$$

where $\text{div} = \frac{1}{\epsilon} + \ln(4\pi) - \gamma_\epsilon$, $L = \ln \left(\frac{\mu^2}{m_1 m_2} \right)$ and m_1, m_2 are the fermion masses in the loop. For $m_1 = m_2 \equiv m$ the expressions for $\Pi_{V\pm A}^{(\prime)}$ are given by

$$\Pi_{V+A} = -m^2 \text{div} - m^2 \ln \left(\frac{\mu^2}{m^2} \right), \quad \Pi_{V-A} = m^2 \text{div} + m^2 \ln \left(\frac{\mu^2}{m^2} \right) \quad (\text{A12})$$

$$\Pi'_{V+A} = \frac{1}{3} \text{div} + \frac{1}{3} \ln \left(\frac{\mu^2}{m^2} \right) - \frac{1}{6}, \quad \Pi'_{V-A} = \frac{1}{6}. \quad (\text{A13})$$

One should note that in [108] the identical expressions have been found in the context of generic model with vectorlike fermions, with the exception of two errors/typos in the expressions for Π'_{V+A} given by Eqs. (A10) and (A13). The modification of Π'_{V+A} presented in [108] such that $L \rightarrow L/3$ in addition to squaring the denominator of the third term gives results identical to our independent calculation. We assume these mistakes are typos as taking the limit of their complete expression for Π'_{V+A} gives rise to a further divergence, and the equal mass limit presented in [108] has inconsistent dimensionality.

For the model with vectorlike fermions ($g_V = 1, g_A = 0$) such as MFDM, the expressions for S and T observables are given in terms of

$$\Pi_V^{(\prime)} = \Pi_{V+A}^{(\prime)} + \Pi_{V-A}^{(\prime)}, \quad (\text{A14})$$

which follows from Eq. (A7). Using Eqs. (A8)–(A13) and Eq. (A14), one finds the following expressions for S and T observables for MFDM:

$$S = \frac{1}{\pi} [\cos^2 \theta \Pi'_V(M_{D'}, M_D) + \sin^2 \theta \Pi'_V(M_{D'}, M_{D_2}) - \Pi'_V(M_+, M_+)], \quad (\text{A15})$$

$$T = \frac{1}{4\pi M_W^2 s_W^2} [\Pi_V(M_+, M_{D'}) + \cos^2 \theta \Pi_V(M_+, M_D) + \sin^2 \theta \Pi_V(M_+, M_{D_2}) - \Pi_V(M_+, M_+) - \cos^2 \theta \Pi_V(M_{D'}, M_D) - \sin^2 \theta \Pi_V(M_{D'}, M_{D_2})], \quad (\text{A16})$$

where θ is the $\chi^0\text{-}\chi_s^0$ mixing angle defined by Eq. (11). The coefficients in front of Π and Π' functions in Eqs. (A15), (A16) are defined by the Lagrangian of MFDM model (7), the complete set of Feynman rules for which is given in HEPMDB.

Recalling that $M_+ = M_{D'}$ from Eq. (A16) it follows that

$$T \equiv 0. \quad (\text{A17})$$

This important feature of MFDM takes place because one of the down parts of the vectorlike doublet, corresponding to the neutral Majorana fermion, does not mix and has the same mass as the charged fermion. For the same reason

$$U \equiv 0 \quad (\text{A18})$$

for MFDM. One should also note that for the expressions for S , T , and U observables both div and $\ln(\mu^2)$ terms cancel out as expected, confirming the consistency and correctness of our evaluation.

APPENDIX B: PROCESS $e^+e^- \rightarrow Z \rightarrow DD_2 \rightarrow DDZ$

One more process leading to the production of D -odd particles at ILC is also observable at $M_{D_2} + M_D < \sqrt{s}$ (in particular, at $\frac{\sqrt{s}}{2} > M_+ > M_{D_2}$):

$$e^+e^- \rightarrow Z \rightarrow DD_2 \rightarrow DDZ. \quad (\text{B1})$$

This process has a clear signature in the modes suitable for observation:

The e^+e^- or $\mu^+\mu^-$ pair with large \cancel{E}_T and large $M(\cancel{E}_T) + \text{nothing}$. The effective mass of this dilepton is $\leq M_Z$, its energy is typically less than $\frac{\sqrt{s}}{2}$.

(B2a)

A quark dijet with large \cancel{E}_T and large $M(\cancel{E}_T) + \text{nothing}$. The effective mass of this dijet is $\leq M_Z$, its energy is typically less than $\frac{\sqrt{s}}{2}$.

(B2b)

At $M_{D_2} < M_+$ the BR for channel with signature (B2a) is 0.06, for the channel with signature (B2b)—0.7. We skip channel $Z \rightarrow \tau^+\tau^-$ with BR = 0.03, 20% of decays of Z are invisible ($Z \rightarrow \nu\bar{\nu}$).

At $M_{D_2} > M_+$ BR's for processes with signature (B2) become less, since new decay channels $D_2 \rightarrow D^\mp W^\pm \rightarrow DW^+W^-$ are added with signature:

$e^+e^- \rightarrow DD_2 \rightarrow DDW^+W^-$: Two quark dijets or dijet + single lepton or two leptons in one hemisphere with large \cancel{E}_T and large $M(\cancel{E}_T) + \text{nothing}$. The effective mass of this system is $\leq M_Z$, its energy is typically less than $\frac{\sqrt{s}}{2}$.

(B3)

The cross section of the process $e^+e^- \rightarrow DD_2$ is model dependent. In the IDM it is determined unambiguously, in MSSM result depends on mixing angles and on the nature of fermions D and D_2 (Dirac or Majorana). In all considered cases at $\sqrt{s} > 200$ GeV this cross section is smaller than $0.1\sigma_0$. Since the BR for events with signature (B2a) is 0.06, at the 500 fb^{-1} luminosity the number of events with this signature is of the order of 10^3 which is not enough for high precision measurements [but certain limits on the masses can be obtained (cf. [51–53] for LEP)].

Nevertheless we describe, for completeness, the energy distributions of Z in this process. The obtained equations are similar to (33)–(36) for new kinematics.

The γ factor and velocity of D_2 in c.m.s. for e^+e^- are

$$\gamma_{D_2} = \frac{s + M_{D_2}^2 - M_D^2}{2\sqrt{s}M_{D_2}},$$

$$\beta_{D_2} = \frac{\sqrt{(s^2 - M_{D_2}^2 - M_D^2)^2 - 4M_D^2M_{D_2}^2}}{s + M_{D_2}^2 - M_D^2}. \quad (\text{B4})$$

For production of Z with an effective mass M_Z^* ($M_Z^* = M_Z$ at $M_{D_2} - M_D > M_Z$ and $M_Z^* \leq M_{D_2} - M_D$ at $M_{D_2} - M_D < M_Z$) in the rest frame of D_2

$$E_Z^D = \frac{M_{D_2}^2 + M_Z^{*2} - M_D^2}{2M_{D_2}},$$

$$p_Z^D = \frac{\sqrt{(M_{D_2}^2 - M_Z^{*2} - M_D^2)^2 - 4M_D^2M_Z^{*2}}}{2M_{D_2}}. \quad (\text{B5})$$

At $M_{D_2} - M_D > M_Z$ the Z -boson energy E_Z lies within the interval with edges

$$E_Z^{(-)} = \gamma_{D_2}(E_Z^D - \beta_{D_2}|\vec{p}|_Z^D), \quad E_Z^{(+)} = \gamma_{D_2}(E_Z^D + \beta_{D_2}|\vec{p}|_Z^D). \quad (\text{B6})$$

At $M_{D_2} - M_D < M_Z$ similar equations are valid for each value of M_Z^* . Absolute upper and lower edges of the energy distribution of Z are reached at $M_Z^* = 0$:

$$E_Z^{(\pm)} = \gamma_{D_2}(1 \pm \beta_{D_2})(M_{D_2}^2 - M_D^2)/(2M_{D_2}). \quad (\text{B7})$$

The peak in the energy distribution of dilepton appears at $M_Z^* = M_{D_2} - M_D$:

$$E_Z = \gamma_{D_2}(M_{D_2} - M_D). \quad (\text{B8})$$

At first sight, measurement of kinematical edges of the dilepton spectrum (B6) (at $M_{D_2} - M_D > M_Z$) gives two equations for M_D and M_{D_2} , allowing for determination of these masses. At $M_{D_2} - M_D < M_Z$, the same procedure can be performed separately for each value of the effective mass of dilepton [109]. In the latter case, the absolute edges of the dilepton energy spectrum (B7) and the position of the peak in this spectrum (B8) could be also used for measuring M_D and M_{D_2} .

In any case, the upper edge in the dijet energy spectrum $E_Z^{(+)}$ (B6), (B7) [signature (B2)] gives one equation, necessary to find M_{D_2} and M_D . In principle, necessary additional information gives position of lower edge in the dilepton energy spectrum $E_Z^{(-)}$. However, as it was noted above, the anticipated number of events with signature (B2a) looks insufficient for obtaining precise results. Together with good results for M_D and M_+ , one can hope to find an accurate value of M_{D_2} .

APPENDIX C: DERIVATIONS

1. E_μ end point: E_μ^{\max}

In this section we present the derivation for the maximum muon energy, E_μ^{\max} , which is achieved when the mass of virtual W boson M_W^* reaches its maximum value of $M_+ - M_D$. We start with the muon energy in the laboratory frame:

$$E_\mu = \gamma_W(1 + c_1\beta_W)(M_W^*/2), \quad (\text{C1})$$

where c_1 is $\cos\theta_1$ of the escape angle of μ relative to the direction of the W in the laboratory frame. We then substitute the γ_W and β_W variables for the edge, given by

$$\gamma_W = E_W/M_W^* = E(1 - M_D/M_+)/M_W^*, \quad (\text{C2})$$

$$\beta_W = \sqrt{1 - M_W^{*2}/E_W^2} = \sqrt{1 - \frac{M_W^{*2}}{E^2(1 - M_D/M_+)^2}} \quad (\text{C3})$$

into Eq. (C1), which gives an E_μ for the off-shell W boson case:

$$E_\mu = \frac{E(1 - M_D/M_+)}{M_W^*} \left(1 + c_1 \sqrt{1 - \frac{M_W^{*2}}{E^2(1 - M_D/M_+)^2}} \right) \times (M_W^*/2). \quad (\text{C4})$$

By substituting $M_W^* = M_+ - M_D$ for the maximum value of M_W^* into Eq. (C4) and setting c_1 to +1 corresponding to the

maximum in E_μ , this gives the maximum edge in muon energy,

$$E_\mu^{\max} = E \frac{(1 - M_D/M_+)}{M_+ - M_D} \left(1 + \sqrt{1 - \frac{(M_+ - M_D)^2}{E^2(1 - \frac{M_D}{M_+})^2}} \right) \times \left(\frac{M_+ - M_D}{2} \right). \quad (\text{C5})$$

Simplifying this down to

$$E_\mu^{\max} = \frac{E(1 - \frac{M_D}{M_+})}{2} \left(1 + \sqrt{1 - \left(\frac{M_+ - M_D}{E(1 - \frac{M_D}{M_+})} \right)^2} \right), \quad (\text{C6})$$

it follows that

$$E_\mu^{\max} = \frac{E(1 - \frac{M_D}{M_+})}{2} (1 + \beta_+), \quad (\text{C7})$$

where $\beta_+ = \sqrt{1 - (\frac{M_+}{E})^2}$.

2. E_μ^\pm derivations

In this section we present the derivation for the upper (+) and lower (-) kinks of the muon energy distribution E_μ , defined as E_μ^\pm . We start with the muon energy in the laboratory frame:

$$E_\mu = \gamma_W(1 + c_1\beta_W) \left(\frac{M_W^*}{2} \right), \quad (\text{C8})$$

where we can substitute $\gamma_W^{(\pm)}$ and $\beta_W^{(\pm)}$ variables in terms of the upper and lower kinks of E_W , defined as

$$\gamma_W^{(\pm)} = \frac{E_W^{(\pm)}}{M_W^*}, \quad (\text{C9})$$

$$\beta_W^{(\pm)} = \sqrt{1 - \left(\frac{M_W^*}{E_W^{(\pm)}} \right)^2}. \quad (\text{C10})$$

We substitute these into E_μ , Eq. (C8), and set c_1 to ± 1 to give the maximum and minimum muon energy kinks $E_\mu^{(\pm)}$ in terms of $E_W^{(\pm)}$:

$$E_\mu^{(\pm)} = \frac{E_W^{(\pm)}}{M_W^*} \left(1 \pm \sqrt{1 - \left(\frac{M_W^*}{E_W^{(\pm)}} \right)^2} \right) \left(\frac{M_W^*}{2} \right). \quad (\text{C11})$$

After simplifying this down, this gives

$$E_\mu^{(\pm)} = \frac{E_W^{(\pm)}}{2} \pm \frac{1}{2} \sqrt{E_W^{(\pm)2} - M_W^{*2}}. \quad (\text{C12})$$

3. Simultaneous equations procedure for finding M_+ and M_D

In this section we present the derivation for the DM masses M_+ and M_D , as a function of the muon energy upper and lower bounds E_μ^\pm , that can be determined independent of each other. Equations (36) and (40) are used to give two simultaneous equations:

$$\frac{4E_\mu^{(+2)} + M_W^2}{4E_\mu^{(+)}} = \frac{E}{M_+} \left(\frac{M_+^2 + M_W^2 - M_D^2}{2M_+} + \sqrt{1 - \frac{M_+^2}{E^2} \frac{\sqrt{M_+^4 + M_W^4 + M_D^4 - 2M_+^2 M_W^2 - 2M_+^2 M_D^2 - 2M_W^2 M_D^2}}{2M_+}} \right), \quad (\text{C13})$$

$$\frac{4E_\mu^{(-2)} + M_W^2}{4E_\mu^{(-)}} = \frac{E}{M_+} \left(\frac{M_+^2 + M_W^2 - M_D^2}{2M_+} - \sqrt{1 - \frac{M_+^2}{E^2} \frac{\sqrt{M_+^4 + M_W^4 + M_D^4 - 2M_+^2 M_W^2 - 2M_+^2 M_D^2 - 2M_W^2 M_D^2}}{2M_+}} \right). \quad (\text{C14})$$

Performing the simultaneous equations procedure gives the equation of M_D in terms of M_+ :

$$M_D^2 = M_W^2 - M_+^2 \left[\frac{1}{E} \left(\frac{4E_\mu^{(+2)} + M_W^2}{4E_\mu^{(+)}} + \frac{4E_\mu^{(-2)} + M_W^2}{4E_\mu^{(-)}} \right) - 1 \right] \quad (\text{C15})$$

and substituting this onto the first simultaneous equation (C13) results in the polynomial of M_+ :

$$-M_+^4 (\alpha + \beta)^2 + 4M_+^2 E^2 (\alpha\beta + M_W^2) - 4M_W^2 E^4 = 0, \quad (\text{C16})$$

where

$$\alpha = \frac{4E_\mu^{(+2)} + M_W^2}{4E_\mu^{(+)}} , \quad \beta = \frac{4E_\mu^{(-2)} + M_W^2}{4E_\mu^{(-)}} . \quad (\text{C17})$$

This gives 4 roots for M_+ :

$$M_+ = \pm \sqrt{2} \sqrt{\frac{-\sqrt{E^4 (\alpha^2 - M_W^2) (\beta^2 - M_W^2)} + \alpha\beta E^2 + E^2 M_W^2}{(\alpha + \beta)^2}}, \quad (\text{C18})$$

$$M_+ = \pm \sqrt{2} \sqrt{\frac{\sqrt{E^4 (\alpha^2 - M_W^2) (\beta^2 - M_W^2)} + \alpha\beta E^2 + E^2 M_W^2}{(\alpha + \beta)^2}}. \quad (\text{C19})$$

Two of these roots will be positive and the top equation will correspond to the physical mass of D^\pm . By rearranging the equation of M_D in terms of M_+ we obtain the following equation for M_D :

$$-\left(\frac{M_W^2 - M_D^2}{\alpha + \beta - E} \right)^2 (\alpha + \beta)^2 + 4 \frac{M_W^2 - M_D^2}{\alpha + \beta - E} E (\alpha\beta + M_W^2) - 4M_W^2 E^2 = 0, \quad (\text{C20})$$

which gives two real and two complex roots for M_D . Out of the two real roots, one is positive and gives the physical mass for D .

- | | |
|---|--|
| <p>[1] G. Jungman, M. Kamionkowski, and K. Griest, Supersymmetric dark matter, <i>Phys. Rep.</i> 267, 195 (1996).</p> <p>[2] U. Ellwanger, C. Hugonie, and A. M. Teixeira, The next-to-minimal supersymmetric standard model, <i>Phys. Rep.</i> 496, 1 (2010).</p> <p>[3] G. Giudice and A. Romanino, Split supersymmetry, <i>Nucl. Phys.</i> B699, 65 (2004); B706, 487(E) (2005).</p> | <p>[4] S. Dodelson and L. M. Widrow, Sterile-Neutrinos as Dark Matter, <i>Phys. Rev. Lett.</i> 72, 17 (1994).</p> <p>[5] M. Cirelli, N. Fornengo, and A. Strumia, Minimal dark matter, <i>Nucl. Phys.</i> B753, 178 (2006).</p> <p>[6] J.E. Kim and G. Carosi, Axions and the strong CP problem, <i>Rev. Mod. Phys.</i> 82, 557 (2010); 91, 049902(E) (2019).</p> |
|---|--|

- [7] H.-C. Cheng, J. L. Feng, and K. T. Matchev, Kaluza-Klein Dark Matter, *Phys. Rev. Lett.* **89**, 211301 (2002).
- [8] D. Hooper and S. Profumo, Dark matter and collider phenomenology of universal extra dimensions, *Phys. Rep.* **453**, 29 (2007).
- [9] C. Boehm and P. Fayet, Scalar dark matter candidates, *Nucl. Phys.* **B683**, 219 (2004).
- [10] G. Branco, P. Ferreira, L. Lavoura, M. Rebelo, M. Sher, and J. P. Silva, Theory and phenomenology of two-Higgs-doublet models, *Phys. Rep.* **516**, 1 (2012).
- [11] A. Belyaev, G. Cacciapaglia, I. P. Ivanov, F. Rojas-Abatte, and M. Thomas, Anatomy of the inert two Higgs doublet model in the light of the LHC and non-LHC dark matter searches, *Phys. Rev. D* **97**, 035011 (2018).
- [12] N. D. Christensen and D. Salmon, New method for the spin determination of dark matter, *Phys. Rev. D* **90**, 014025 (2014).
- [13] A. Belyaev, L. Panizzi, A. Pukhov, and M. Thomas, Dark matter characterization at the LHC in the effective field theory approach, *J. High Energy Phys.* **04** (2017) 110.
- [14] M. Asano, T. Saito, T. Suehara, K. Fujii, R. S. Hundi, H. Itoh, S. Matsumoto, N. Okada, Y. Takubo, and H. Yamamoto, Discrimination of new physics models with the international linear collider, *Phys. Rev. D* **84**, 115003 (2011).
- [15] N. D. Christensen, T. Han, Z. Qian, J. Sayre, J. Song, and Stefanus, Determining the dark matter particle mass through antler topology processes at lepton colliders, *Phys. Rev. D* **90**, 114029 (2014).
- [16] M. Burns, K. Kong, K. T. Matchev, and M. Park, Using subsystem MT2 for complete mass determinations in decay chains with missing energy at hadron colliders, *J. High Energy Phys.* **03** (2009) 143.
- [17] A. M. Sirunyan *et al.* (CMS Collaboration), Search for new physics in final states with an energetic jet or a hadronically decaying W or Z boson and transverse momentum imbalance at $\sqrt{s} = 13$ TeV, *Phys. Rev. D* **97**, 092005 (2018).
- [18] M. Aaboud *et al.* (ATLAS Collaboration), Search for dark matter and other new phenomena in events with an energetic jet and large missing transverse momentum using the ATLAS detector, *J. High Energy Phys.* **01** (2018) 126.
- [19] A. M. Sirunyan *et al.* (CMS Collaboration), Search for dark matter produced with an energetic jet or a hadronically decaying W or Z boson at $\sqrt{s} = 13$ TeV, *J. High Energy Phys.* **07** (2017) 014.
- [20] A. M. Sirunyan *et al.* (CMS Collaboration), Search for dark matter and unparticles in events with a Z boson and missing transverse momentum in proton-proton collisions at $\sqrt{s} = 13$ TeV, *J. High Energy Phys.* **03** (2017) 061; **09** (2017) 106(E).
- [21] M. Aaboud *et al.* (ATLAS Collaboration), Search for dark matter in events with a hadronically decaying vector boson and missing transverse momentum in pp collisions at $\sqrt{s} = 13$ TeV with the ATLAS detector, *J. High Energy Phys.* **10** (2018) 180.
- [22] A. Basalaev (ATLAS Collaboration), Search for dark matter particle candidates produced in association with a Z boson in pp collisions at a center-of-mass energy of 13 TeV with the ATLAS detector, *J. Phys. Conf. Ser.* **934**, 012024 (2017).
- [23] M. Aaboud *et al.* (ATLAS Collaboration), Search for an invisibly decaying Higgs boson or dark matter candidates produced in association with a Z boson in pp collisions at $\sqrt{s} = 13$ TeV with the ATLAS detector, *Phys. Lett. B* **776**, 318 (2018).
- [24] M. Aaboud *et al.* (ATLAS Collaboration), Search for dark matter at $\sqrt{s} = 13$ TeV in final states containing an energetic photon and large missing transverse momentum with the ATLAS detector, *Eur. Phys. J. C* **77**, 393 (2017).
- [25] A. M. Sirunyan *et al.* (CMS Collaboration), Search for dark matter produced in association with a Higgs boson decaying to $\gamma\gamma$ or $\tau^+\tau^-$ at $\sqrt{s} = 13$ TeV, *J. High Energy Phys.* **09** (2018) 046.
- [26] A. M. Sirunyan *et al.* (CMS Collaboration), Search for associated production of dark matter with a Higgs boson decaying to $b\bar{b}$ or $\gamma\gamma$ at $\sqrt{s} = 13$ TeV, *J. High Energy Phys.* **10** (2017) 180.
- [27] ATLAS Collaboration, Search for Dark Matter Produced in association with a Higgs boson decaying to $b\bar{b}$ at $\sqrt{s} = 13$ TeV with the ATLAS detector using 79.8 fb^{-1} of proton-proton collision data, Report No. ATLAS-CONF-2018-039, 2018.
- [28] M. Aaboud *et al.* (ATLAS Collaboration), Search for dark matter in association with a Higgs boson decaying to two photons at $\sqrt{s} = 13$ TeV with the ATLAS detector, *Phys. Rev. D* **96**, 112004 (2017).
- [29] G. Aad *et al.* (ATLAS Collaboration), Search for Dark Matter in Events with Missing Transverse Momentum and a Higgs Boson Decaying to Two Photons in pp Collisions at $\sqrt{s} = 8$ TeV with the ATLAS Detector, *Phys. Rev. Lett.* **115**, 131801 (2015).
- [30] A. M. Sirunyan *et al.* (CMS Collaboration), Search for Dark Matter Particles Produced in Association with a Top Quark Pair at $\sqrt{s} = 13$ TeV, *Phys. Rev. Lett.* **122**, 011803 (2019).
- [31] A. M. Sirunyan *et al.* (CMS Collaboration), Search for dark matter in events with energetic, hadronically decaying top quarks and missing transverse momentum at $\sqrt{s} = 13$ TeV, *J. High Energy Phys.* **06** (2018) 027.
- [32] M. Aaboud *et al.* (ATLAS Collaboration), Search for dark matter produced in association with bottom or top quarks in $\sqrt{s} = 13$ TeV pp collisions with the ATLAS detector, *Eur. Phys. J. C* **78**, 18 (2018).
- [33] A. M. Sirunyan *et al.* (CMS Collaboration), Search for invisible decays of a Higgs boson produced through vector boson fusion in proton-proton collisions at $\sqrt{s} = 13$ TeV, *Phys. Lett. B* **793**, 520 (2019).
- [34] M. Aaboud *et al.* (ATLAS Collaboration), Combination of Searches for Invisible Higgs Boson Decays with the ATLAS Experiment, *Phys. Rev. Lett.* **122**, 231801 (2019).
- [35] A. M. Sirunyan *et al.* (CMS Collaboration), Search for narrow and broad dijet resonances in proton-proton collisions at $\sqrt{s} = 13$ TeV and constraints on dark matter mediators and other new particles, *J. High Energy Phys.* **08** (2018) 130.
- [36] A. M. Sirunyan *et al.* (CMS Collaboration), Search for new physics in dijet angular distributions using proton-proton

- collisions at $\sqrt{s} = 13$ TeV and constraints on dark matter and other models, *Eur. Phys. J. C* **78**, 789 (2018).
- [37] A. M. Sirunyan *et al.* (CMS Collaboration), Search for dijet resonances in proton-proton collisions at $\sqrt{s} = 13$ TeV and constraints on dark matter and other models, *Phys. Lett. B* **769**, 520 (2017); **772**, 882(E) (2017).
- [38] J. R. Ellis, T. Falk, K. A. Olive, and M. Schmitt, Constraints on neutralino dark matter from LEP-2 and cosmology, *Phys. Lett. B* **413**, 355 (1997).
- [39] M. Aaboud *et al.* (ATLAS Collaboration), Search for long-lived charginos based on a disappearing-track signature in pp collisions at $\sqrt{s} = 13$ TeV with the ATLAS detector, *J. High Energy Phys.* **06** (2018) 022.
- [40] A. M. Sirunyan *et al.* (CMS Collaboration), Search for disappearing tracks as a signature of new long-lived particles in proton-proton collisions at $\sqrt{s} = 13$ TeV, *J. High Energy Phys.* **08** (2018) 016.
- [41] M. Aaboud *et al.* (ATLAS Collaboration), Search for long-lived, massive particles in events with displaced vertices and missing transverse momentum in $\sqrt{s} = 13$ TeV pp collisions with the ATLAS detector, *Phys. Rev. D* **97**, 052012 (2018).
- [42] A. M. Sirunyan *et al.* (CMS Collaboration), Search for long-lived particles with displaced vertices in multijet events in proton-proton collisions at $\sqrt{s} = 13$ TeV, *Phys. Rev. D* **98**, 092011 (2018).
- [43] D. Barducci, A. Belyaev, A. K. M. Bharucha, W. Porod, and V. Sanz, Uncovering natural supersymmetry via the interplay between the LHC and direct dark matter detection, *J. High Energy Phys.* **07** (2015) 066.
- [44] P. Athron *et al.* (GAMBIT Collaboration), A global fit of the MSSM with GAMBIT, *Eur. Phys. J. C* **77**, 879 (2017).
- [45] P. Athron *et al.* (GAMBIT Collaboration), Combined collider constraints on neutralinos and charginos, *Eur. Phys. J. C* **79**, 395 (2019).
- [46] I. F. Ginzburg, Measuring mass and spin of dark matter particles with the aid energy spectra of single lepton and dijet at the e^+e^- linear collider, *J. Mod. Phys.* **5**, 1036 (2014).
- [47] N. G. Deshpande and E. Ma, Pattern of symmetry breaking with two Higgs doublets, *Phys. Rev. D* **18**, 2574 (1978).
- [48] R. Barbieri, L. J. Hall, and V. S. Rychkov, Improved naturalness with a heavy Higgs: An alternative road to LHC physics, *Phys. Rev. D* **74**, 015007 (2006).
- [49] I. F. Ginzburg, K. A. Kanishev, M. Krawczyk, and D. Sokolowska, Evolution of Universe to the present inert phase, *Phys. Rev. D* **82**, 123533 (2010).
- [50] M. Gustafsson, S. Rydbeck, L. Lopez-Honorez, and E. Lundstrom, Status of the inert doublet model and the role of multileptons at the LHC, *Phys. Rev. D* **86**, 075019 (2012).
- [51] M. Espirito-Santo, K. Hultqvist, P. Johansson, and A. Lipniacka, Search for neutralino pair production at \sqrt{s} from 192 to 208 gev, Report No. DELPHI-2003-002, 2003.
- [52] E. Lundström, M. Gustafsson, and J. Edsjö, Inert doublet model and LEP II limits, *Phys. Rev. D* **79**, 035013 (2009).
- [53] M. Aoki, S. Kanemura, and H. Yokoya, Reconstruction of inert doublet scalars at the international linear collider, *Phys. Lett. B* **725**, 302 (2013).
- [54] E. Ma, Verifiable radiative seesaw mechanism of neutrino mass and dark matter, *Phys. Rev. D* **73**, 077301 (2006).
- [55] R. Barbieri, L. J. Hall, and V. S. Rychkov, Improved naturalness with a heavy Higgs: An alternative road to LHC physics, *Phys. Rev. D* **74**, 015007 (2006).
- [56] L. Lopez Honorez, E. Nezri, J. F. Oliver, and M. H. Tytgat, The inert doublet model: An archetype for dark matter, *J. Cosmol. Astropart. Phys.* **02** (2007) 028.
- [57] C. Arina, F.-S. Ling, and M. H. G. Tytgat, IDM and iDM or the inert doublet model and inelastic dark matter, *J. Cosmol. Astropart. Phys.* **10** (2009) 018.
- [58] E. Nezri, M. H. G. Tytgat, and G. Vertongen, e^+ and anti- p from inert doublet model dark matter, *J. Cosmol. Astropart. Phys.* **04** (2009) 014.
- [59] X. Miao, S. Su, and B. Thomas, Tripleton signals in the inert doublet model, *Phys. Rev. D* **82**, 035009 (2010).
- [60] M. Gustafsson, S. Rydbeck, L. Lopez-Honorez, and E. Lundstrom, Status of the inert doublet model and the role of multileptons at the LHC, *Phys. Rev. D* **86**, 075019 (2012).
- [61] A. Arhrib, R. Benbrik, and N. Gaur, $H \rightarrow \gamma\gamma$ in inert Higgs doublet model, *Phys. Rev. D* **85**, 095021 (2012).
- [62] B. Swiezewska and M. Krawczyk, Diphoton rate in the inert doublet model with a 125 GeV Higgs boson, *Phys. Rev. D* **88**, 035019 (2013).
- [63] A. Goudelis, B. Herrmann, and O. Stl, Dark matter in the inert doublet model after the discovery of a Higgs-like boson at the LHC, *J. High Energy Phys.* **09** (2013) 106.
- [64] A. Arhrib, Y.-L. S. Tsai, Q. Yuan, and T.-C. Yuan, An updated analysis of inert Higgs doublet model in light of the recent results from LUX, PLANCK, AMS-02 and LHC, *J. Cosmol. Astropart. Phys.* **06** (2014) 030.
- [65] M. Krawczyk, D. Sokolowska, P. Swaczyna, and B. Swiezewska, Constraining inert dark matter by $R_{\gamma\gamma}$ and WMAP data, *J. High Energy Phys.* **09** (2013) 055.
- [66] M. Krawczyk, D. Sokolowska, P. Swaczyna, and B. Swiezewska, Higgs $\rightarrow \gamma\gamma$, $Z\gamma$ in the inert doublet model, *Acta Phys. Pol. B* **44**, 2163 (2013).
- [67] A. Ilnicka, M. Krawczyk, and T. Robens, Inert doublet model in light of LHC run I and astrophysical data, *Phys. Rev. D* **93**, 055026 (2016).
- [68] M. A. D-az, B. Koch, and S. Urrutia-Quiroga, Constraints to dark matter from inert Higgs doublet model, *Adv. High Energy Phys.* **2016**, 8278375 (2016).
- [69] K. P. Modak and D. Majumdar, Confronting galactic and extragalactic γ -rays observed by Fermi-lat with annihilating dark matter in an inert Higgs doublet model, *Astrophys. J. Suppl. Ser.* **219**, 37 (2015).
- [70] F. S. Queiroz and C. E. Yaguna, The CTA aims at the inert doublet model, *J. Cosmol. Astropart. Phys.* **02** (2016) 038.
- [71] C. Garcia-Cely, M. Gustafsson, and A. Ibarra, Probing the inert doublet dark matter model with Cherenkov telescopes, *J. Cosmol. Astropart. Phys.* **02** (2016) 043.
- [72] M. Hashemi and S. Najjari, Observability of inert scalars at the LHC, *Eur. Phys. J. C* **77**, 592 (2017).

- [73] P. Poulou, S. Sahoo, and K. Sridhar, Exploring the inert doublet model through the dijet plus missing transverse energy channel at the LHC, *Phys. Lett. B* **765**, 300 (2017).
- [74] A. Alves, D. A. Camargo, A. G. Dias, R. Longas, C. C. Nishi, and F. S. Queiroz, Collider and dark matter searches in the inert doublet model from Peccei-Quinn symmetry, *J. High Energy Phys.* **10** (2016) 015.
- [75] A. Datta, N. Ganguly, N. Khan, and S. Rakshit, Exploring collider signatures of the inert Higgs doublet model, *Phys. Rev. D* **95**, 015017 (2017).
- [76] E. Aprile *et al.* (XENON Collaboration), Dark Matter Search Results from a One Ton-Year Exposure of XENON1T, *Phys. Rev. Lett.* **121**, 111302 (2018).
- [77] R. Enberg, P. J. Fox, L. J. Hall, A. Y. Papaioannou, and M. Papucci, LHC and dark matter signals of improved naturalness, *J. High Energy Phys.* **11** (2007) 014.
- [78] T. Cohen, J. Kearney, A. Pierce, and D. Tucker-Smith, Singlet-doublet dark matter, *Phys. Rev. D* **85**, 075003 (2012).
- [79] A. Belyaev, N. D. Christensen, and A. Pukhov, CalcHEP 3.4 for collider physics within and beyond the Standard Model, *Comput. Phys. Commun.* **184**, 1729 (2013).
- [80] A. Semenov, LanHEP—A package for automatic generation of Feynman rules from the Lagrangian. Version 3.2, *Comput. Phys. Commun.* **201**, 167 (2016).
- [81] <https://hepmdb.soton.ac.uk>, High Energy Physics Models DataBase (HEPMDB), webpage, 2011.
- [82] <https://hepmdb.soton.ac.uk/hepmdb:0420.0327>.
- [83] G. Belanger, F. Boudjema, A. Pukhov, and A. Semenov, micrOMEGAs: A tool for dark matter studies, *Nuovo Cimento C* **033N2**, 111 (2010).
- [84] D. Dercks, N. Desai, J. S. Kim, K. Rolbiecki, J. Tattersall, and T. Weber, CheckMATE 2: From the model to the limit, *Comput. Phys. Commun.* **221**, 383 (2017).
- [85] A. M. Sirunyan *et al.* (CMS Collaboration), Search for electroweak production of charginos and neutralinos in multilepton final states in proton-proton collisions at $\sqrt{s} = 13$ TeV, *J. High Energy Phys.* **03** (2018) 166.
- [86] M. E. Peskin and T. Takeuchi, Estimation of oblique electroweak corrections, *Phys. Rev. D* **46**, 381 (1992).
- [87] R. L. Workman *et al.* (Particle Data Group), Review of Particle Physics (1978), <https://pdg.lbl.gov/2022/>.
- [88] M. J. G. Veltman, Limit on Mass Differences in the Weinberg Model, *Nucl. Phys. B* **123**, 89 (1977).
- [89] M. S. Chanowitz, M. A. Furman, and I. Hinchliffe, Weak Interactions of Ultraheavy Fermions, *Phys. Lett. B* **78**, 285 (1978).
- [90] T. Abe *et al.* (Linear Collider ILC Concept Group—Collaboration), The international large detector: Letter of intent, [arXiv:1006.3396](https://arxiv.org/abs/1006.3396).
- [91] T. Sjöstrand, S. Ask, J. R. Christiansen, R. Corke, N. Desai, P. Ilten, S. Mrenna, S. Prestel, C. O. Rasmussen, and P. Z. Skands, An introduction to PYTHIA8.2, *Comput. Phys. Commun.* **191**, 159 (2015).
- [92] J. de Favereau, C. Delaere, P. Demin, A. Giammanco, V. Lemaître, A. Mertens, and M. Selvaggi (DELPHES 3 Collaboration), DELPHES 3, A modular framework for fast simulation of a generic collider experiment, *J. High Energy Phys.* **02** (2014) 057.
- [93] M. Cacciari, G. P. Salam, and G. Soyez, The anti- k_r jet clustering algorithm, *J. High Energy Phys.* **04** (2008) 063.
- [94] C. Patrignani *et al.* (Particle Data Group Collaboration), Review of particle physics, *Chin. Phys. C* **40**, 100001 (2016).
- [95] J. A. Aguilar-Saavedra *et al.* (ECFA/DESY LC Physics Working Group Collaboration), TESLA: The superconducting electron positron linear collider with an integrated x-ray laser laboratory. Technical design report. Part 3. Physics at an e^+e^- linear collider, [arXiv:hep-ph/0106315](https://arxiv.org/abs/hep-ph/0106315).
- [96] H. Baer, T. Logan, A. Nomerotski, M. Perelstein, M. E. Peskin, R. Pöschl, J. Reuter, S. Riemann, A. Savoy-Navarro, G. Servant, T. M. P. Tait, and J. Yu, The international linear collider technical design report—volume 2: Physics, [arXiv:1306.6352](https://arxiv.org/abs/1306.6352).
- [97] Y. Li and A. Nomerotski, Chargino and neutralino masses at ILC, in *Proceedings of the International Linear Collider Workshop* (2010), [arXiv:1007.0698](https://arxiv.org/abs/1007.0698).
- [98] M. Asano, T. Saito, T. Suehara, K. Fujii, R. S. Hundi, H. Itoh, S. Matsumoto, N. Okada, Y. Takubo, and H. Yamamoto, Discrimination of new physics models with the international linear collider, *Phys. Rev. D* **84**, 115003 (2011).
- [99] H. Abramowicz *et al.* (ILD Concept Group Collaboration), International large detector: Interim design report, [arXiv:2003.01116](https://arxiv.org/abs/2003.01116).
- [100] G. Moortgat-Pick, LHC/ILC interplay in SUSY searches, *J. Phys. Conf. Ser.* **110**, 072027 (2008).
- [101] A. Freitas, H. U. Martyn, U. Nauenberg, and P. M. Zerwas, Sleptons: Masses, mixings, couplings, 2004.
- [102] J. A. Conley, H. K. Dreiner, and P. Wienemann, Measuring a light neutralino mass at the ILC: Testing the MSSM neutralino cold dark matter model, *Phys. Rev. D* **83**, 055018 (2011).
- [103] M. Skrzypek and S. Jadach, Exact and approximate solutions for the electron nonsinglet structure function in QED, *Z. Phys. C* **49**, 577 (1991).
- [104] P. Chen, Differential luminosity under multi-photon beamstrahlung, *Phys. Rev. D* **46**, 1186 (1992).
- [105] L. Bian, J. Shu, and Y. Zhang, Prospects for triple gauge coupling measurements at future lepton colliders and the 14 TeV LHC, *J. High Energy Phys.* **09** (2015) 206.
- [106] J. De Blas, G. Durieux, C. Grojean, J. Gu, and A. Paul, On the future of Higgs, electroweak and diboson measurements at lepton colliders, *J. High Energy Phys.* **12** (2019) 117.
- [107] R. Barbieri, A. Pomarol, R. Rattazzi, and A. Strumia, Electroweak symmetry breaking after LEP-1 and LEP-2, *Nucl. Phys. B* **703**, 127 (2004).
- [108] G. Cynolter and E. Lendvai, Electroweak precision constraints on vector-like fermions, *Eur. Phys. J. C* **58**, 463 (2008).
- [109] I. F. Ginzburg, Simple and robust method for search dark matter particles and measuring their properties at ILC in various models of DM, *Proc. Sci., QFHEP2010* (2010) 028 [[arXiv:1010.5579](https://arxiv.org/abs/1010.5579)].